



Contents lists available at ScienceDirect

Journal of Rock Mechanics and Geotechnical Engineering

journal homepage: www.jrmge.cn



Full Length Article

Complex spatial and size distributions of landslides in the Yarlung Tsangpo River (YTR) basin



Bo Zhao ^a, Lijun Su ^{a, b, c,*}

^a State Key Laboratory of Mountain Hazards and Engineering Resilience, and Institute of Mountain Hazards and Environment, Chinese Academy of Sciences, Chengdu, 610041, China

^b China-Pakistan Joint Research Center on Earth Sciences, Islamabad, Pakistan

^c University of Chinese Academy of Sciences, Beijing, 100049, China

ARTICLE INFO

Article history:

Received 27 November 2023

Received in revised form

19 January 2024

Accepted 31 January 2024

Available online 28 May 2024

Keywords:

Landslides

Yarlung tsangpo river (YTR)

Asymmetric distribution

Tsangpo suture zone

Alternating hard and soft rock groups

ABSTRACT

The Yarlung Tsangpo River (YTR), located in the Himalayan orogenic belt, is renowned for its deep gorges and complex tectonic features, as well as its reputation as a landslide-prone region. However, less is known about the distribution of landslides across the entire river basin. To address this gap in knowledge, this study first established a comprehensive landslide inventory across the entire basin using remote sensing mapping and multiple field investigations. Then, a systematic analysis of the spatial and size distributions was conducted. The results indicated that the YTR basin features at least 2390 landslides with areas exceeding 10^4 m^2 , spanning a total area and volume of 1087.6 km^2 and 48.4 km^3 , respectively. These landslides can be classified into eight types, and rockslides are the most common (53.1%). Their distributions are highly asymmetric, with the following notable patterns: (1) the Tsangpo suture zone (53.4%) contains a greater number of landslides than other tectonic units; (2) the landslide size is influenced by the relief and elevation conditions, with positive relationships observed between the local relief and landslide area, as well as between the elevation range and landslide area; and (3) the landslide distribution is not significantly correlated with rainfall, and seasonally frozen ground is associated with a greater concentration of landslides. Alternating slate and shale groups in the Tsangpo suture zone may be the factors responding to landslide concentration. A total of 20.6% of landslide-blocked rivers were observed, with some forming river knickpoints. Due to the limited data, spatial and size analyses are perhaps immature, and further systematic analysis remains necessary.

© 2025 Institute of Rock and Soil Mechanics, Chinese Academy of Sciences. Published by Elsevier B.V. This is an open access article under the CC BY-NC-ND license (<http://creativecommons.org/licenses/by-nc-nd/4.0/>).

1. Introduction

Landslides are downslope movements of rock, soil, or both on mountain slopes (Highland and Bobrowsky, 2008). In some extreme cases, landslides can cross kilometer-scale distances at geologically instantaneous times (about 10^2 s), resulting in river blockages and house burials; tectonically active mountain belts (i.e. Andes belt, Alps belt) and orogenic plateau margins (i.e. Tibetan Plateau) are usually landslide-prone areas (Keefer, 2002; Wen et al.,

2004; Zhou et al., 2013; Wang et al., 2018; Bloom et al., 2020; Zhao et al., 2021a, 2023a). Landslides have long been recognized as important contributors to regional mountain erosional budgets, and they can also limit mountain relief in tectonically active mountain belts; additionally, their spatial distributions and magnitudes are important indicators of landscape evolution (Hovius et al., 1997; Malamud et al., 2004; Korup, 2005, 2006; Korup et al., 2007; Brideau et al., 2009; Ouimet, 2010; Roering, 2012; Larsen and Montgomery, 2012; Marc et al., 2019; Carlini et al., 2018; Zhao, 2024). The spatial and size distributions of landslides in a specific area or basin could provide valuable insights into the regional evolution process.

It is widely accepted that the Tibetan Plateau, especially at its margins, is a typical landslide-prone area, and river basins are usually treated as study areas (Korup et al., 2007; Korup and Montgomery, 2008; Zhao, 2020; Zhou et al., 2021; Wang et al.,

* Corresponding author. State Key Laboratory of Mountain Hazards and Engineering Resilience, and Institute of Mountain Hazards and Environment, Chinese Academy of Sciences, Chengdu 610041, China.

E-mail address: sulijun1976@163.com (L. Su).

Peer review under responsibility of Institute of Rock and Soil Mechanics, Chinese Academy of Sciences.

2023). Landslides in basins usually exhibit asymmetric distributions and are strongly related to local geological, topographic and climatic conditions (Carlini et al., 2016; Zhao, 2020; Zhao et al., 2021b). For example, the Diexi area is a famous landslide-prone area in Minjiang River basin on the eastern Tibetan Plateau. This area is formed in the Jiaochang arcuate belt, with alternating layers of soft and hard rock, and a deep-cutting gorge caused by rapid river erosion (Zhao, 2020; Zhao et al., 2021b). A similar scenario has also been observed in the Basu Basin of the Nujiang River Basin, the Luding area of the Dadu River Basin, the Batang area of the Jinshajiang River Basin, and the Nanga Parbat–Haramosh Massif in the Indus Basin. (Hewitt, 2009; Jia et al., 2020; Zeng et al., 2021).

Basin-wide landslide analyses have been carried out on many rivers in the Tibetan Plateau, such as the Minjiang River, Bailong River, Dadu River, Jinsha River, and Indus River (Korup et al., 2007, 2010; Wu, 2013; Zhao, 2020; Zhao et al., 2019a; Zhou et al., 2021). However, no study has evaluated the famous Yarlung Tsangpo River (YTR), except for some case studies, such as the 2000 Yigong landslide and Lulang landslide (Delaney and Evans, 2015; Zhou et al., 2016; Han, 2018; Wang et al., 2019; Guo et al., 2020; Hu et al., 2021). The YTR is located in the eastern Himalayan Mountain belt on the southern margin of the Qinghai-Tibetan Plateau and is characterized by high elevation, high relief, intensive tectonic activity and erosion, especially in the Himalayan syntaxis (Holt et al., 1991; Finnegan et al., 2008; Korup and Montgomery, 2008; Korup et al., 2010; Lang et al., 2013; Zhao et al., 2021c). Currently, landslide distribution analysis in the YTR has focused on the eastern Himalayan syntaxis; for example, Larsen and Montgomery (2012) established a long-term landslide inventory of the eastern Himalayan syntaxis and revealed that landslide erosion rates are significantly correlated with exhumation rates and stream power and that small increases in mean hillslope angles above 30° translate into large and significant increases in landslide erosion. Zhao et al. (2019b, 2021c, 2023b) established a landslide inventory triggered by the 2017 M_s -6.9 Nyingchi earthquake and analyzed its spatial and size distributions.

Given the absence of regional-scale studies on the geomorphic signatures of large landslides or the roles of geology and topography in their distribution, this study aimed to (1) establish a landslide inventory, (2) reveal complex spatial and size distributions, and (3) discuss possible controls on the landslide distribution, as well as the geomorphologic response to landslides.

2. Background of the YTR basin

Since approximately 50 million years ago, the collision of the Indian and Eurasian Plates has made the Qinghai-Tibetan Plateau uplift continuously (Yin and Harrison, 2000). The continuous northward movement of the Indian Plate has made the Qinghai-Tibetan Plateau a tectonically active region that contains eight subfault blocks (Deng et al., 2014), forming numerous suture zones and active faults (Pan et al., 2002). The southern margin of the Qinghai-Tibetan Plateau is the well-known Himalayan orogenic belt, and two suture zones also exist in this region, i.e. the Tsangpo and Eurasian-Indian suture zones (Fig. 1a; Zhao et al., 2010). The Himalayan orogenic belt is also an earthquake-prone area, and many mega-earthquakes, such as the 1950 Chayu M_w -8.6 earthquake, the 2005 Kashmir M_w -7.6 earthquake, the 2015 Nepal M_w -7.9 earthquake, and the 2017 Nyingchi M_w -6.4 earthquake, have occurred either in or near the YTR basin (Fig. 1a; Elliott et al., 2016; Zhao et al., 2021c, 2023b). The data indicate that at least 800 seismic events with magnitudes (M_w) ≥ 3.0 have occurred in the basin since the 1900s. Furthermore, the magnitudes of 17 events were ≥ 6.0 . The largest event was a M_w -7.4 event, which occurred in 1952 (Fig. A1a in Appendix A).

The YTR originates from the central Himalayan orogenic belt, and the mainstream extends eastward along the Tsangpo suture zone, with a length exceeding 2000 km (Fig. 1a and b). According to the tectonic unit distributions of the Tibetan Plateau, the entire basin lies in the Himalayan orogenic belt (VII) and the detailed subtectonic units of the Ladake-Gangdise-Chayu Lake basin system (VII₁), Tsangpo suture zone (VII₃), and Himalayan block (VII₄, Fig. A1a in Appendix A; Pan et al., 2002). The eastern Himalayan syntaxis lies in the eastern segment of the basin (Fig. 1b). The regional principal stress direction is perpendicular to the (mainstream) river extension (Heidbach et al., 2018). According to the Code for the Investigation of Geotechnical Engineering, China (GB 50021-2001, 2009; the detailed classification criteria are shown in Table A1 in Appendix A), the basin comprises four rock groups, i.e. hard rock, secondary hard rock, alternating soft and hard rock, and soft rock (Fig. A1b in Appendix A).

The basin area is approximately 2.5×10^5 km². The mean, maximum and minimum elevations of the YTR basin are approximately 4635 m, 7800 m and 430 m, respectively. The YTR basin is characterized by local relief values ranging from 10 m to 4540 m, and the mean local relief is approximately 1050 m (local relief is defined as the maximum elevation difference based on the 30 m resolution digital elevation model (DEM) in a moving window with a 10-km radius; Korup et al., 2010; Fig. A1c in Appendix A). The YTR profile also shows that the source is more than 5000 m above sea level (m.a.s.l.), and the endpoint is < 200 m.a.s.l. within the basin, and the maximum elevation difference is approximately 5400 m (Fig. A1c in Appendix A). Glaciers (4.8%), permafrost regions (29.7%) and seasonally frozen ground (65.5%) are distributed within the basin (Liu et al., 2020; Ran et al., 2021); glaciers and permafrost regions are located mainly along the basin boundaries, especially in the downstream region, while seasonally frozen ground is found in relatively low river valleys (Fig. A1d in Appendix A). Additionally, the mean annual precipitation (MAP) shows a nonuniform distribution, and the lower stream is part of a typical high-precipitation area, especially for the eastern Himalayan syntaxis, whose annual rainfall exceeds 2500 mm/year (Fig. A1e in Appendix A).

3. Methods

3.1. Landslide mapping

Landslides are composed of the material that detaches from mountain slopes; subsequently, they move downward and accumulate at slope feet or lower positions on slopes (Cruden and Varnes, 1996; Highland and Bobrowsky, 2008; Hung et al., 2014; Xu et al., 2023). Thus, one important scenario of landslides, especially large landslides, is that obvious concave reliefs or tension cracks are present in the upper slope, and convex deposits are present at the slope foot or in the lower section (Cruden and Varnes, 1996; Highland and Bobrowsky, 2008).

In this study, Google Earth was used to map all traceable landslides in an area of 257,000 km² (Fig. 2a). Google Earth provided satellite-derived images with resolutions less than 1.0 m over the entire study area, and it also provided 3D views, which were used to identify landslides more easily. This study adopted a manual visual interpretation method to perform landslide mapping. The landslide mapping process follows:

- (1) Landslide identification was carried out for every subbasin;
- (2) If a suspected case was found, a systematic evaluation was carried out based on the topographic features, land cover, etc. The landslide boundary was recognized by topographic differences (i.e. concave cavities in the source area and raised landforms in the deposit area).

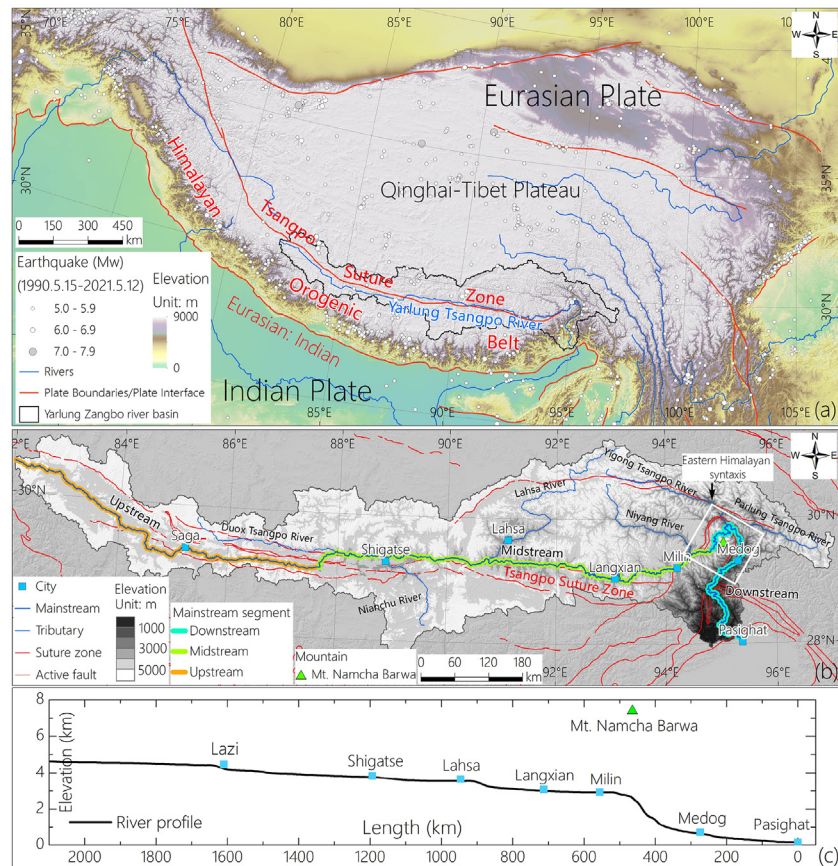


Fig. 1. Location and background of the YTR basin. (a) Location and tectonic setting, (b) topography and suture zone, and (c) mainstream profile. The plate boundary/plate interface and historical earthquake data were from the United States Geological Survey (USGS, 2023a, b), and the suture zones and active faults were derived from Pan et al. (2002).

Table 1
Landslide size statistics of different landslide types.

Landslide type	Landslide number	Total number of landslides (%)	Total landslide area (km ²)	Mean landslide area (km ²)
RS	1270	53.1	454.5	0.343
RA	281	11.8	224.2	0.792
MRF	127	5.3	39.7	0.298
ISA	5	0.2	54.4	10.9
DS	46	1.9	17.8	0.371
ES	31	1.3	13.7	0.429
CL	435	18.2	241.2	0.551
SD	195	8.2	42.6	0.208

(3) The entire landslide boundary was drawn in Google Earth once the boundary was confirmed.

All the work lasted for several years, and multiple field investigations were carried out to verify the mapping accuracy and reveal the field characteristics of landslides. In addition, because many landslides are ancient landslides whose boundaries are not very clear, we estimated them based on our comprehensive understanding. This study mainly focused on landslides with areas larger than 10⁴ m² because these landslides are usually considered deep-seated landslides and important agents of landscape evolution that can cause extensive and rapid topographic changes (Görüm, 2019; Pánek et al., 2021). In addition, in this study, multitemporal Sentinel images (10 m resolution, 1 January 2017 to 31 December 2021) were used to identify historical glacial avalanches in Sedongpu gully (for a detailed discussion, see Section 5.2.2).

During the landslide interpretation process, we also matched

the landslides with the 1:200,000 geological maps to obtain the geological features of the landslide (such as the rock type and strata attitude). Then, the updated Varnes classification scheme and field conditions were adopted to classify the observed landslides (Cruden and Varnes, 1996; Hung et al., 2014), and eight landslide types were distinguished, including rockslides (RSs, both planar and rotational), rock avalanches (RAs), multi-rock falls (MRFs), ice–snow avalanches (ISAs), debris slides (DSs), earthflows (EFs), complex landslides (CLs) and slope deformations (SDs), as shown in Fig. 2b–i. There also exists a special landslide pattern naming complex landslides, especially combinations of multi-rock falls and seasonal snow avalanches in the Parlung Tsangpo River (PTR) basin (Fig. 2h). Slope deformation is also visible in this region and is characterized by large, slow-moving mass movements associated with typical landforms, such as ridge grabens, multiple uphill-facing scarps and bulging toes (Fig. 2i; Agliardi et al., 2001; Pánek et al., 2021). Glacial rock avalanches were also classified as ice/

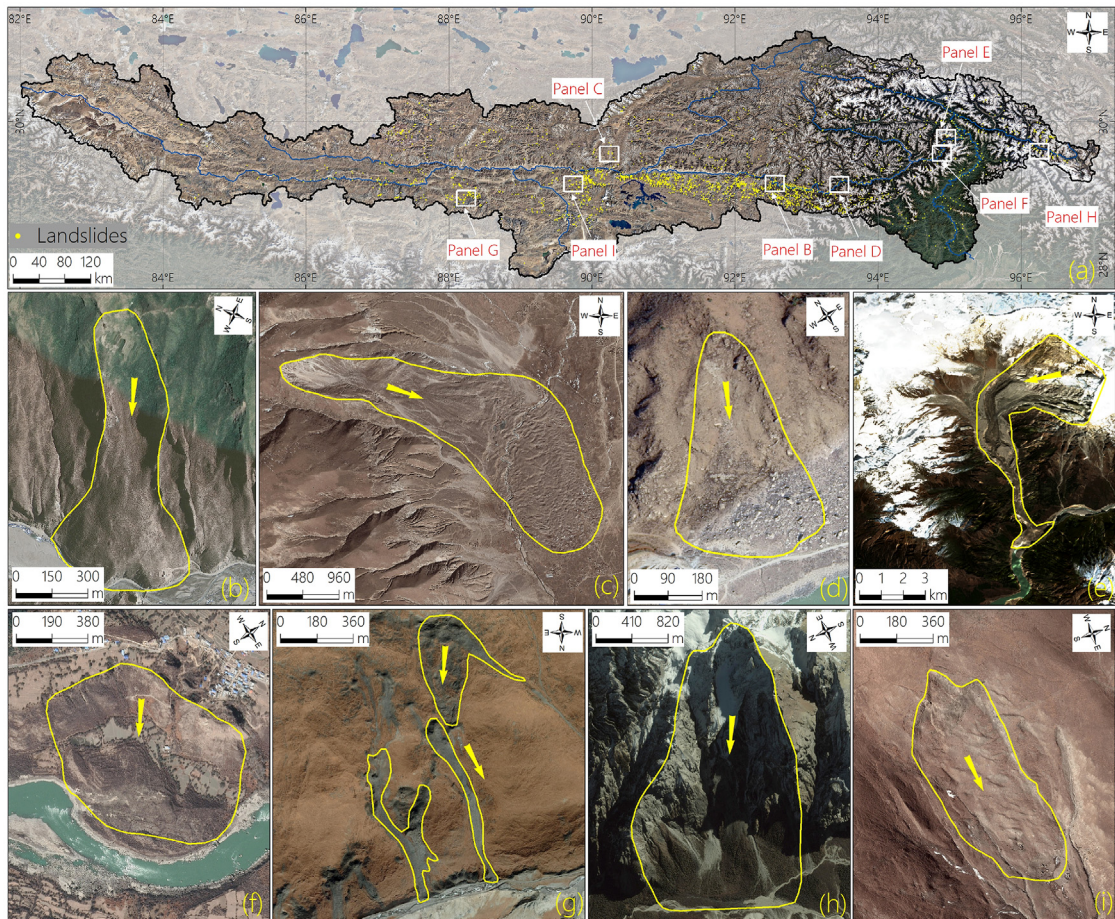


Fig. 2. Landslide mapping in the YTR Basin: (a) spatial distribution of mapped landslides and examples of (b) a rockslide, (c) a rock avalanche, (d) a multi-rock fall, (e) an ice–snow avalanche, (f) a debris slide, (g) an earthflow, (h) a complex landslide, and (i) a slope deformation landslide. The remote sensing images were all obtained from Google Earth.

snow avalanches in this study. In addition, dammed landslides were also recognized during landslide mapping.

3.2. Landslide mapping

3.2.1. Data preparation

According to our previous studies and other relevant studies (Du et al., 2017, 2019, 2021; Zhao et al., 2019b, 2021c, 2023a; Li et al., 2022), geological, topographical and seismic data, as well as climate proxy information, were collected to recognize the factors influencing the spatial and size distributions of landslides.

The geological data including information on tectonic units (Pan et al., 2002), active faults (1:500,000), and geological maps (1:500,000) in the study area are collected. As the river basin is so large that it is difficult to display all the strata, we translated the different strata into rock groups, including hard rock, secondary hard rock, alternating soft and hard rock, and soft rock, according to the Code for the Investigation of Geotechnical Engineering, China (GB 50021-2001, 2009; the classification criteria are listed in Table A1 in Appendix A).

The topographic data include elevation, slope, aspect and local relief. The elevation data were obtained from 30-m resolution DEM that was downloaded from ALOS World 3D (AW3D30, 2024). Slope, aspect and local relief (moving window: 10-km radius) data were both derived from the 30-m resolution DEM on the Geographic Information System (GIS) platform.

The seismic data contained a historical earthquake inventory,

and the historical earthquake inventory covering the entire study area was downloaded from the United States Geological Survey (USGS, 2023b). The inventory contains earthquakes that have occurred since the 1900s with magnitudes (M_w) ≥ 3.0 . Some basic information, including epicenters, magnitude, date, and focal depth, was recorded in this inventory.

The climate data included the mean annual ground temperature (MAGT) from 2005 to 2015 (Zou et al., 2017; Ran et al., 2021), glacial data collected since the mid-20th century (Liu et al., 2020) and mean annual precipitation (MAP) data (2007–2018 period; Brocca et al., 2019). Additionally, an MAGT value ≤ 0 °C indicates permafrost, and an MAGT value > 0 °C indicates seasonally frozen soil, except in the Pasighat area, according to a newly published permafrost distribution map (Zou et al., 2017).

3.2.2. Data analysis

All the regional analyses were performed on the GIS platform. The landslide spatial distribution was displayed using the centroids of source areas. The landslide kernel density was calculated within a 5 km radius to determine the spatial concentration. To illustrate the spatial distributions of different landslide sizes, category classifications (such as classifications of elevation, relief, and slope) were adopted, and joint spatial operation was applied to determine the number of landslides that occurred within specific tectonic units and rock groups. Other statistical data, such as data about landslide elevations, slope angle, local relief, aspect and rainfall were also calculated on the GIS platform. Additionally, to

characterize the relationship between the regional topography and landslide concentration, $10 \text{ km} \times 10 \text{ km}$ cells were established.

To quantitatively analyze the relative position of occurrence on a hill, this study adopted the relative position index r , which defines the ratio of the distance to the valley bottom (L) to the distance from the ridge line to the valley bottom (S) (Zhao et al., 2021c; for details, see Fig. A2 in Appendix A). The different r values represent the different hill sections, i.e. the r values of [0.0–0.2], [0.2–0.4], [0.4–0.6], [0.6–0.8], [0.8–1.0], and [0.9–1.0] represent the lower, lower-middle, middle, upper-middle, upper and top sections, respectively, of a hill (Fig. A2 in Appendix A).

To obtain landslide size distribution, the size–frequency statistic is adopted, which is defined as $p = dN/dA$ (p is the ratio of the landslide number dN to the corresponding landslide area interval dA ; Malamud et al., 2004; Roback et al., 2018; Tebbens, 2020), and its distribution usually exhibits power-law scaling when the landslide size exceeds a specific threshold (Tanyaş et al., 2019; Tebbens, 2020). The formula of the best-fitting power-law function for this study follows $\log_{10} p = \beta \log_{10} A + b$ (β and b are constants), as proposed by Roback et al. (2018). To obtain the best-fitting power-law function for this study, statistical software was used to automatically calculate the constants β and b . Additionally, other trend line formulas were automatically calculated by this software.

4. Spatial and size distributions of landslides

4.1. Landslide inventory

A total of 2390 cases were recognized in the YTR basin, and their spatial distributions are shown in Fig. 3a. For the entire dataset, the mapped landslides include rockslides (RSs), rock avalanches (RAs), multi-rock falls (MRFs), ice–snow avalanches (ISAs), debris slides (DSs), earthflows (EFs), complex landslides (CLs), and slope deformations (SDs),

(SDs), earthflows (EFs), complex landslides (CLs), and slope

deformations (SDs) (Fig. 3b); their basic statistics are listed in Table 1. RSs are the most common type in the YTR (Table 1). The spatial distribution of landslides exhibits an obvious nonuniform distribution with the following characteristics (Fig. 3c):

- (1) The area with the highest landslide density is located in the middle reaches of the YTR;
- (2) The southern segment of the mainstream has a greater concentration of landslides than does the northern segment;
- (3) An important scenario can be observed in the tectonic units, as the Tsangpo suture zone (VII₃) contains the most landslides, especially in the region of the Langjexue accretionary wedge (VII₃₋₂).

To evaluate the landslide volume, this study adopted empirical landslide area–volume scaling relationship for the Himalayas, as proposed by Larsen et al. (2010):

$$V = 0.26A^{1.36} \quad (1)$$

where V is the landslide volume, and A is the landslide area. The 2390 identified landslides span a total area of 1087.6 km^2 , and the average landslide area is 0.46 km^2 . Altogether, the landslides correspond to a volume of 48.4 km^3 .

For the spatial and size distributions of different landslide types (Fig. 4), the RS landslide distribution is similar to that of the total dataset, except in the eastern segment of the basin (Fig. 3a and 4a). Larger RAs are concentrated in the eastern basin with high relief, relatively small RAs are distributed to the south (within 40 km) of the middle reaches (Fig. 4b), and RAs have the second-largest mean landslide area, following ISAs (Fig. 5a and Table 1). ISAs are mainly concentrated in and near the eastern Himalayan syntaxis (Fig. 4b),

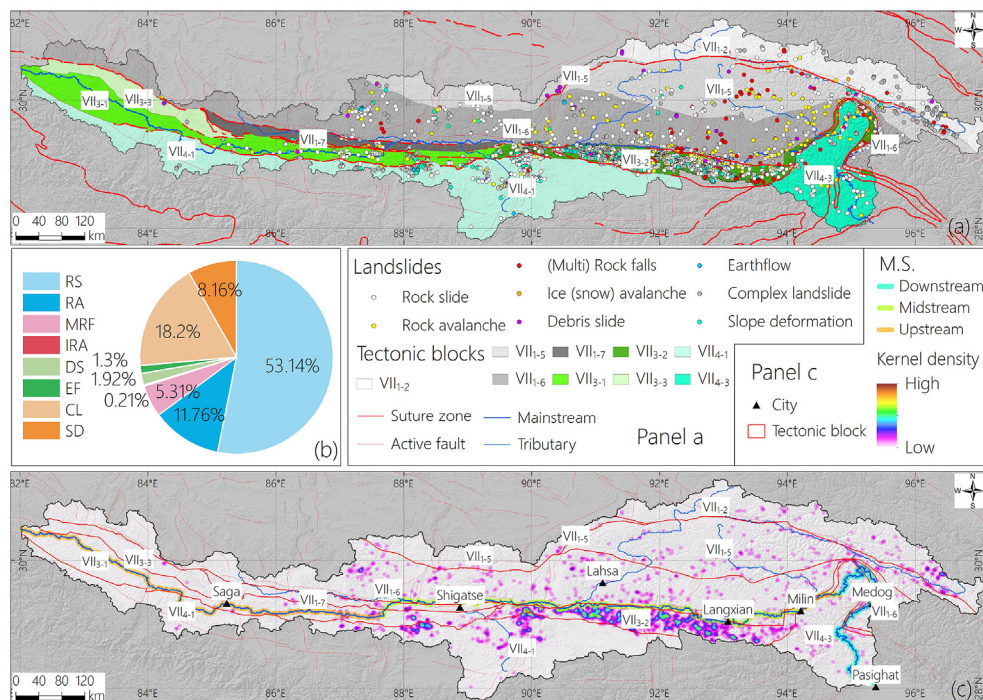


Fig. 3. Landslide distributions in the YTR basin: (a) spatial distribution, (b) proportions of different landslide types, and (c) landslide concentration. M.S. in the legend of Panel Fig. 3c is the mainstream segment. The tectonic units that were used were obtained from Pan et al. (2002); VII – Himalayan orogenic belt, VII₁ – Ladake-Gangdise-Chayu lake basin system, VII₂ – Tsangpo suture zone, VII₄ – Himalayan block, VII₁₋₂ – Anglong-Bange-Tengchong magmatic arc zone, VII₁₋₅ – Jiangda island arc zone, VII₁₋₆ – Chayu magmatic arc zone, VII₁₋₇ – Shigatse forearc basin, VII₃₋₁ – Tsangpo ophiolite mélange zone, VII₃₋₂ – Langjexue accretionary wedge, VII₃₋₃ – Zongba block, VII₄₋₁ – Himalayan passive terrigenous basin, and VII₄₋₃ – High Himalayan basement complex zone.

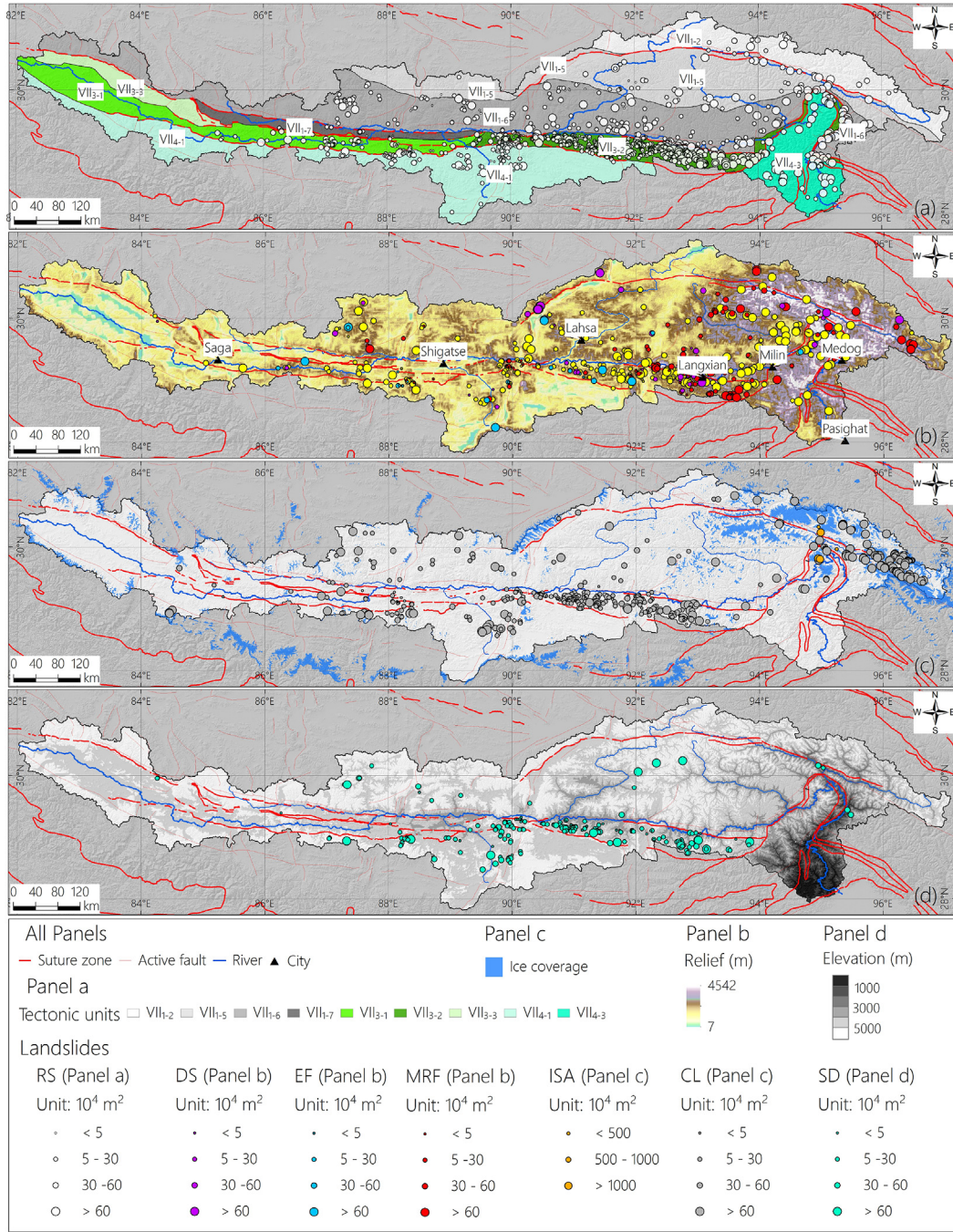


Fig. 4. Spatial and size distributions of different landslide types: (a) rockslides, (b) rock avalanches, multi-rock falls, ice–snow avalanches, debris slides and earthflows, (c) complex landslides, and (d) slope deformations. The glacier coverage data were obtained from Liu et al. (2020).

and ISAs show the largest mean landslide area (Fig. 5a and Table 1). CLs are mainly concentrated in the eastern segment of the basin (which is part of the PTR subbasin) and in zone VII₃₋₂ (Fig. 4c), and the CLs in the PTR basin represent combinations of MRFs and seasonal snow avalanches. SDs are mainly distributed in the middle–upper river reaches, both of which lie in areas with seasonally frozen ground (Fig. 4d; the seasonally frozen ground is defined as ground with mean annual ground temperatures $>0^\circ\text{C}$; for a detailed discussion, see Section 4.4). ISAs and EFs occur at higher elevations than do the other landslide types (Fig. 5b), and the ISAs exhibit the largest vertical drops (Fig. 5c).

RSs have the largest total area of approximately 454.5 km^2 , and

ISAs have the largest mean landslide area of 10.9 km^2 , while the mean landslide areas of the other landslide types are both less than 1 km^2 (Table 1). For the landslide frequency density p , all landslides with an area $\geq 10^6 \text{ m}^2$, which is derived statistically, exhibit a power-law scaling relationship of $\log_{10} p = -2.34 \log_{10} A + 10.7$ (Fig. 6a). The frequency density distributions of the RSs, RAs, CLs and SDs all follow similar formulas with the same β values but different b values (Fig. 6b, c, h and i), and the frequency density distributions of the MRFs, ISAs, DSs and EFs have no such distribution patterns (Fig. 6d–g).

In addition, the YTR basin features mainly deep gorges, especially in the middle–lower reaches, and the eastern Himalayan

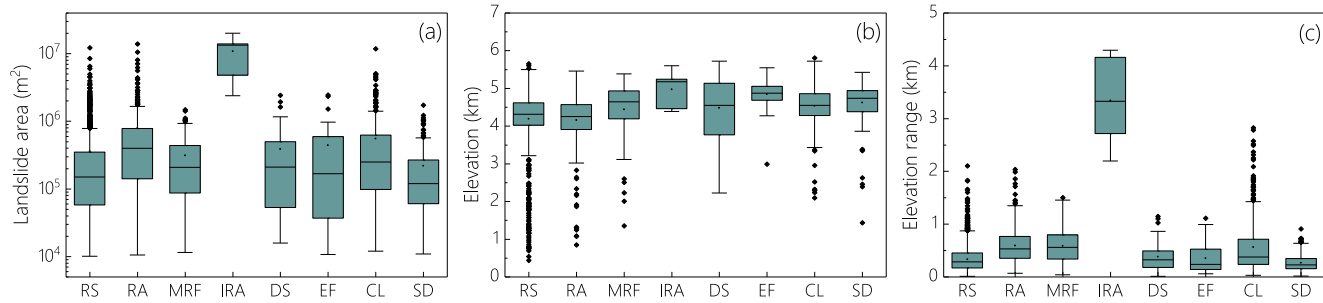


Fig. 5. Statistics of the areas (a), elevations (b) and vertical drops (c) of different landslide types.

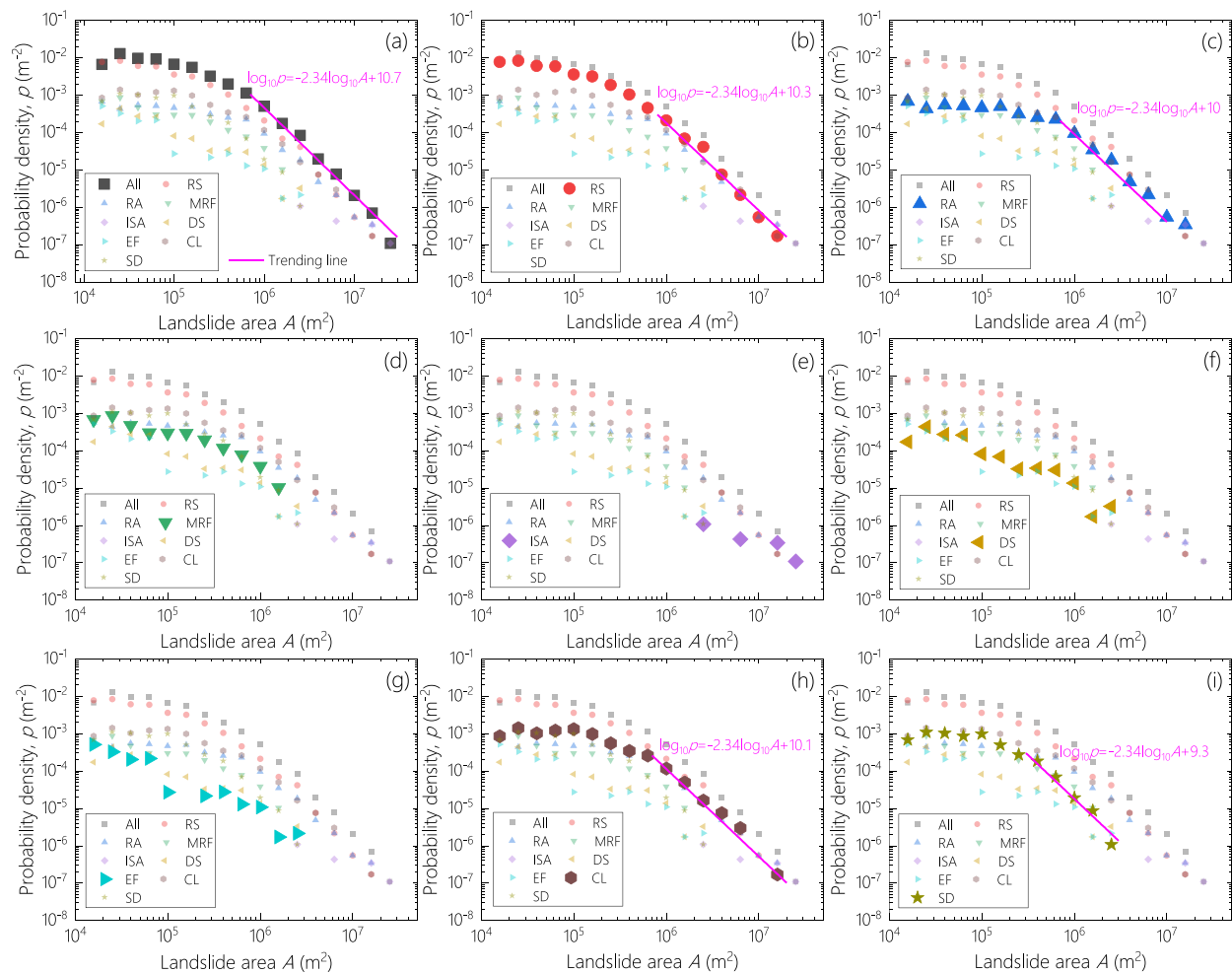


Fig. 6. Size distributions of different landslide types. (a) All landslides, (b) rockslides, (c) rock avalanches, (d) multi-rock falls, (e) ice–snow avalanches, (f) debris slides, (g) earthflows, (h) complex landslides, and (i) slope deformations.

syntaxis is among Earth's deepest bedrock gorges (Korup et al., 2010). Large landslides usually block these gorges due to their limited movement space. Among 2390 identified landslides, 510 (20.6%) were once obviously blocked rivers (termed “landslide damming” herein), and 45 landslides still contained obvious dammed lakes or sediments. The distributions of these landslide types are shown in Fig. 7a and b, respectively. RSs, RAs and CLs makeup almost all damming landslide types (Fig. 7c and d), 60% of the identified ISAs block rivers, and some ISA-induced lake dams remain. All the landslide-dammed lakes are distributed in the

lower reaches, especially within and near the eastern Himalayan syntaxis (Fig. 7b).

4.2. Geological distribution of landslides

The areas affected by landslides are asymmetrically distributed among geological units and rock groups (Figs. 8 and 9). The YTR basin comprises the Ladake-Gangdise-Chayu Lake basin system (VII₁), Tsangpo suture zone (VII₃), and Himalayan block (VII₄), in which 1025, 1277 and 88 landslides, respectively, are concentrated

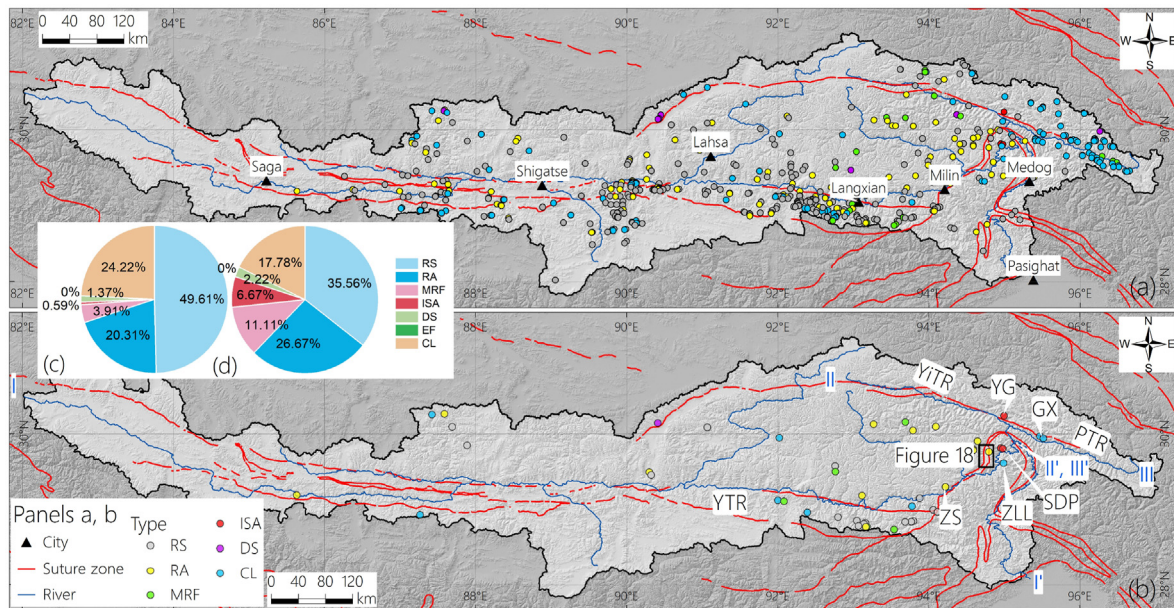


Fig. 7. (a) Distribution of landslide damming, (b) distribution of existing landslide dams, and (c) and (d) corresponding landslide proportions of different landslide types in Fig. 7a and b, respectively. In (b), ZLL – Zelunglung landslide; SDP – Sedongpu landslide; YG – Yigong landslide; GX – Guxiang landslide; ZS – Zhongsa landslide; and I – I', II – II' and III – III' are river profiles, and their results are listed in Fig. 19.

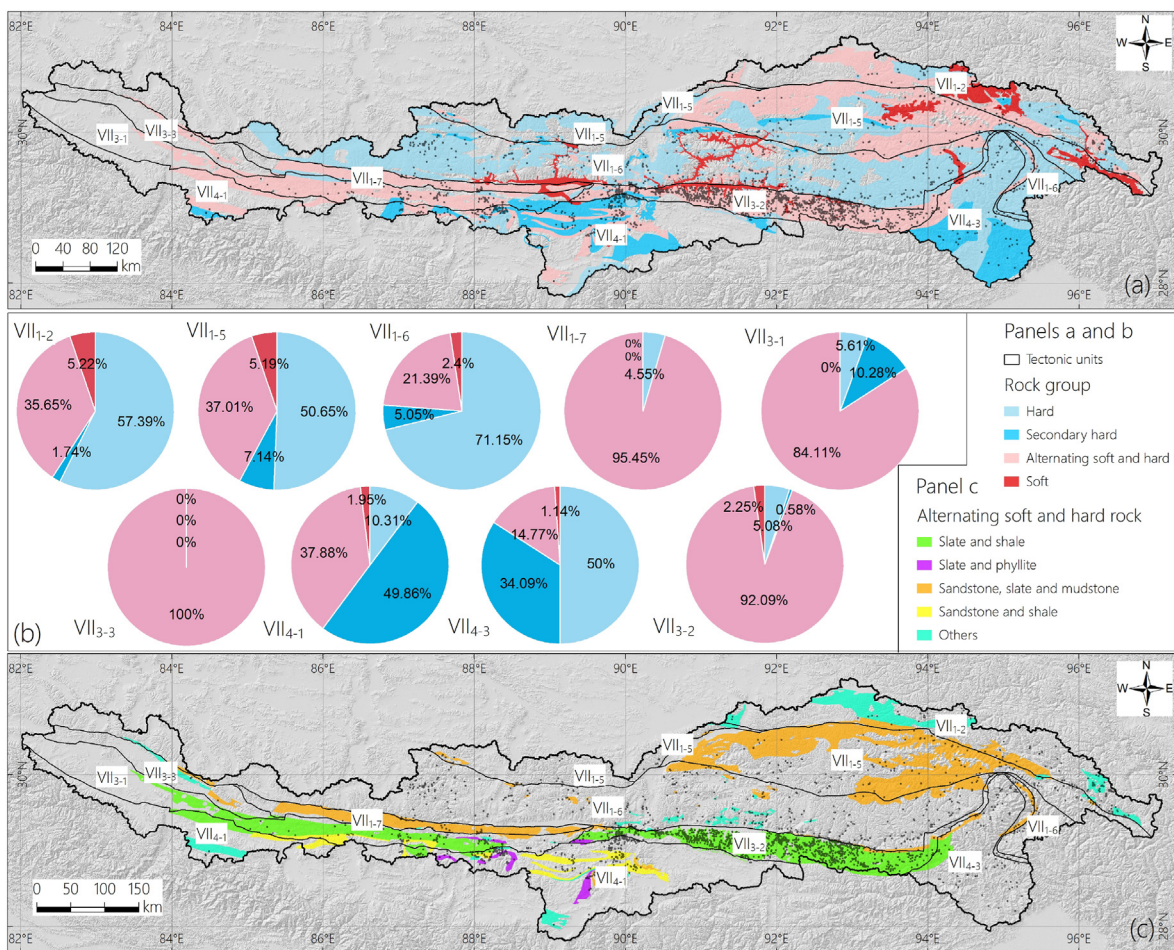


Fig. 8. Spatial distributions of landslides among geological indices. (a) Different rock groups, (b) proportions of landslides related to rock groups in different tectonic units, and (c) detailed compositions of alternating soft and hard rocks. The rock groups were revised from a 500,000 geological map, and the classification criteria are listed in Table A1 in Appendix A.

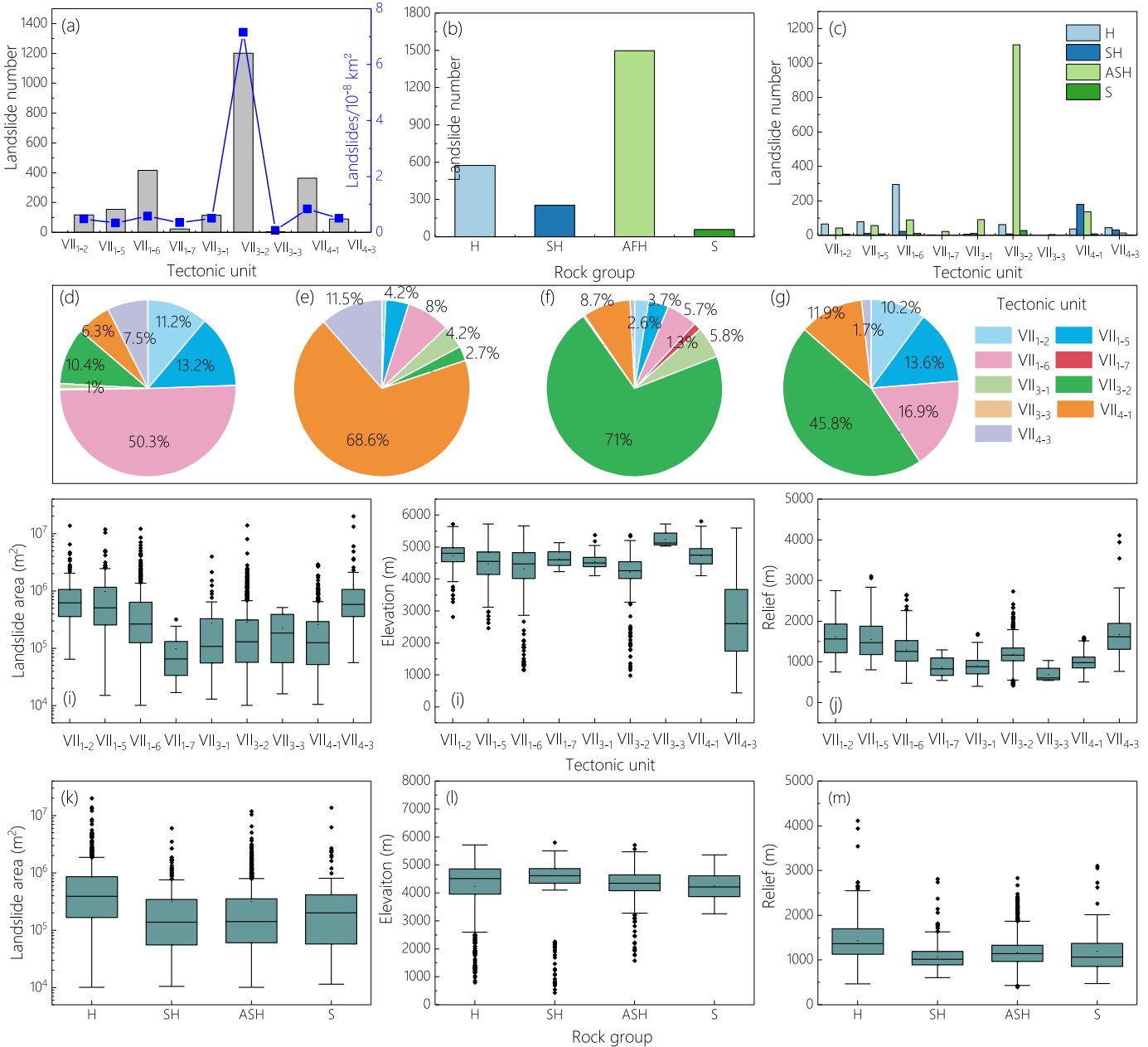


Fig. 9. Statistics of landslide distribution derived based on different geological factors: (a), (b) and (c) distribution of landslide numbers in different tectonic units and rock groups; landslide proportions in different tectonic units under the different rock groups, including hard rock (d), secondary hard rock (e), alternating soft and hard rock (f) and soft rock (g); distributions of landslide areas (h), elevations (i) and local relief conditions (j) in different tectonic units; and distributions of landslide areas (k), elevations (l) and local relief conditions (m) in different rock groups.

in these 3 zones, hosting 42.9%, 53.4% and 3.7% of the total dataset, respectively. Among the subtectonic units, the Langjixue accretionary wedge (VII₃₋₂) contains 1201 landslides that account for 48.6% of the total landslides (Fig. 8a and 9a). Thus, area VII₃₋₂ is a landslide-prone area in the YTR basin. Regarding the rock groups, the hard rock, secondary hard rock, alternating hard and soft rock and soft rock groups contain 573, 253, 1496, and 58 landslides, occupying 24.0%, 10.6%, 62.6% and 2.4% of the total landslides, respectively (Fig. 9b). Thus, alternating hard and soft rocks are part of the landslide-prone rock group in the YTR basin. Among the rocks within the alternating hard and soft rocks, the alternating slate and shale in the Upper Triassic Xiukang Group, which are mainly distributed in the Langjixue accretionary wedge (VII₃₋₂),

contain 1188 landslides, accounting for 49.7% of the total dataset and approximately 92% landslides in zone VII₃₋₂, respectively (Fig. 8c).

Landslides in tectonic units VII₁₋₇ have the minimum mean landslide area, while landslides in tectonic units VII₄₋₃ have the maximum mean landslide area (Fig. 9h). The landslides in tectonic units VII₁₋₇ are also characterized by a lower mean elevation but a high mean local relief (Fig. 9i and j), which could be explained by the regional topographic features of zone VII₄₋₃, which is located downstream of the river and characterized by a lower elevation. Additionally, it is part of the eastern Himalayan syntaxis, which contains some of the deepest incised gorges on Earth (Finnegan et al., 2008; Korup et al., 2010). Furthermore, landslides in the

hard rock group usually exhibit relatively large mean landslide areas and relief characteristics (Fig. 9k and m), while both present similar mean elevations (Fig. 9l).

The proportions of landslides related to rock groups in different tectonic units are different, and the dominant rock groups in tectonic units VII₁₋₇, VII₃₋₂, VII₃₋₂ and VII₃₋₃ are alternating hard and soft rocks. The dominant rock groups in tectonic units VII₁₋₂, VII₁₋₅, VII₁₋₆ and VII₄₋₃ are hard rocks, and the dominant rock group in tectonic unit VII₄₋₁ is secondary hard rocks (Fig. 8b and 9b).

Hard-rock landslides are mainly concentrated in units VII₁₋₆ (Chayu magmatic arc zone; Fig. 9c), secondary hard-rock landslides are mainly concentrated in units VII₄₋₁ (Himalayan passive terrigenous basin; Fig. 9d), and alternating soft- and hard-rock landslides and soft-rock landslides are both mainly concentrated in units VII₃₋₂ (Langjiexue accretionary wedge; Fig. 9f and g).

4.3. Topographic distribution of landslides

Fig. 10 shows the landslide distribution along the east-west profile. As shown in the figure, numerous landslides are concentrated in tributaries rather than in the mainstream YTR, and landslides occurring at elevations of 4000–5000 m account for 68.1% of the total dataset (1627 landslides; Fig. 10a and 11a). Hard-rock landslides experience greater vertical drops and larger areas than other landslide types (Fig. 10b). The eastern Himalayan syntaxis has a greater elevation range than the other sections, and the landslide areas in this section are larger than those in the other sections (Fig. 10b).

There are 1939 landslides that have occurred in local reliefs ranging from 500 to 1500 m, occupying 81.1% of the total (Fig. 10b and 11b). For relative positions of occurrence, higher positions on a slope (larger r values) lead to more landslides; i.e. 479, 748 and 896 landslides are concentrated in the middle section (r : 0.4–0.6), upper–middle section (r : 0.6–0.8) and upper (or top) section (r : 0.8–1.0), occupying 20.1%, 30.3% and 36.3%, respectively (Fig. 11c). The relationship between the landslide elevation and landslide area shows that landslides that occur at higher elevations have wider area ranges, and when the elevation exceeds 4000 m, the landslide

areas increase as the elevation continues to increase (Fig. 11d). The relationship between the local relief and landslide area exhibits an approximately exponential function, i.e. $y = 10^{(0.0023m+1.6)}$ (where m is the local relief and y is the landslide area; Fig. 11e). The relationship between the vertical drop in landslides and landslide area also preliminarily displays an exponential function, i.e. $y = 10^{[(v-10)^{0.21}+1.8]}$ (where v is the landslide elevation range and y is the landslide area; Fig. 11f). Additionally, the east–west direction is the most landslide-prone direction, especially the west direction, and at least 740 landslides have azimuths of 240°–310°, composing 31.0% of the total (Fig. 11g).

For the unit cell (10 km × 10 km) landslide distribution, the highest landslide concentration corresponds to 35 landslides in one cell (Fig. 12a). According to the mean elevation, elevation range and slope statistics of the cells, cells with mean elevations of 3500–5500 m and slopes of 20–30° contain relatively high numbers of landslides, and the highest concentrations of landslides are also within these regions (Fig. 12b). As the grid elevation increases, the mean grid slopes exponentially increase, characterized by $y = (x-600)^{0.46}+1.5$ (where x is the cell elevation range, and y is the mean cell slope), and the elevation range of 1300–2300 m contains more landslides than the other elevation ranges (Fig. 12c).

4.4. Climatic distribution of landslides

In Figs. 13 and 14, most landslide-prone areas, such as zones VII₃₋₁, VII₃₋₂, and VII₃₋₃, can be characterized as seasonally frozen areas (MAGTs > 0 °C), and the middle-lower reaches, especially the Yigong Tsangpo River (YiTR) and PTR, contain widely distributed permafrost and glaciers. The southern section of the mainstream (zone VII₃₋₂) comprises widespread seasonally frozen areas, while the northern section mainly contains permafrost (Fig. 13a). 2198 landslides are concentrated in the seasonally frozen ground area, occupying 90.0% of the total (Fig. 14), and the landslide densities of landslides in the seasonally frozen ground area and permafrost area (including the glacier area) are 0.013 and 0.002 landslide/km², respectively. A potential explanation could be that seasonally frozen ground areas usually undergo more intensive freeze-thaw

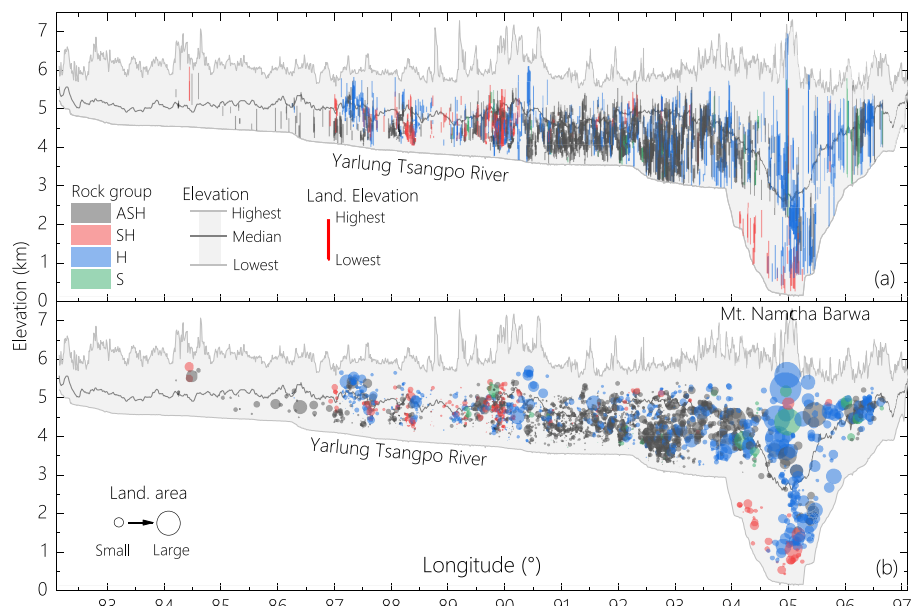


Fig. 10. Distribution of vertical drops in landslides (a) and landslide areas (b) along east-west profiles. The gray shading displays the elevation ranges (vertical drop), while the colors correspond to the rock groups.

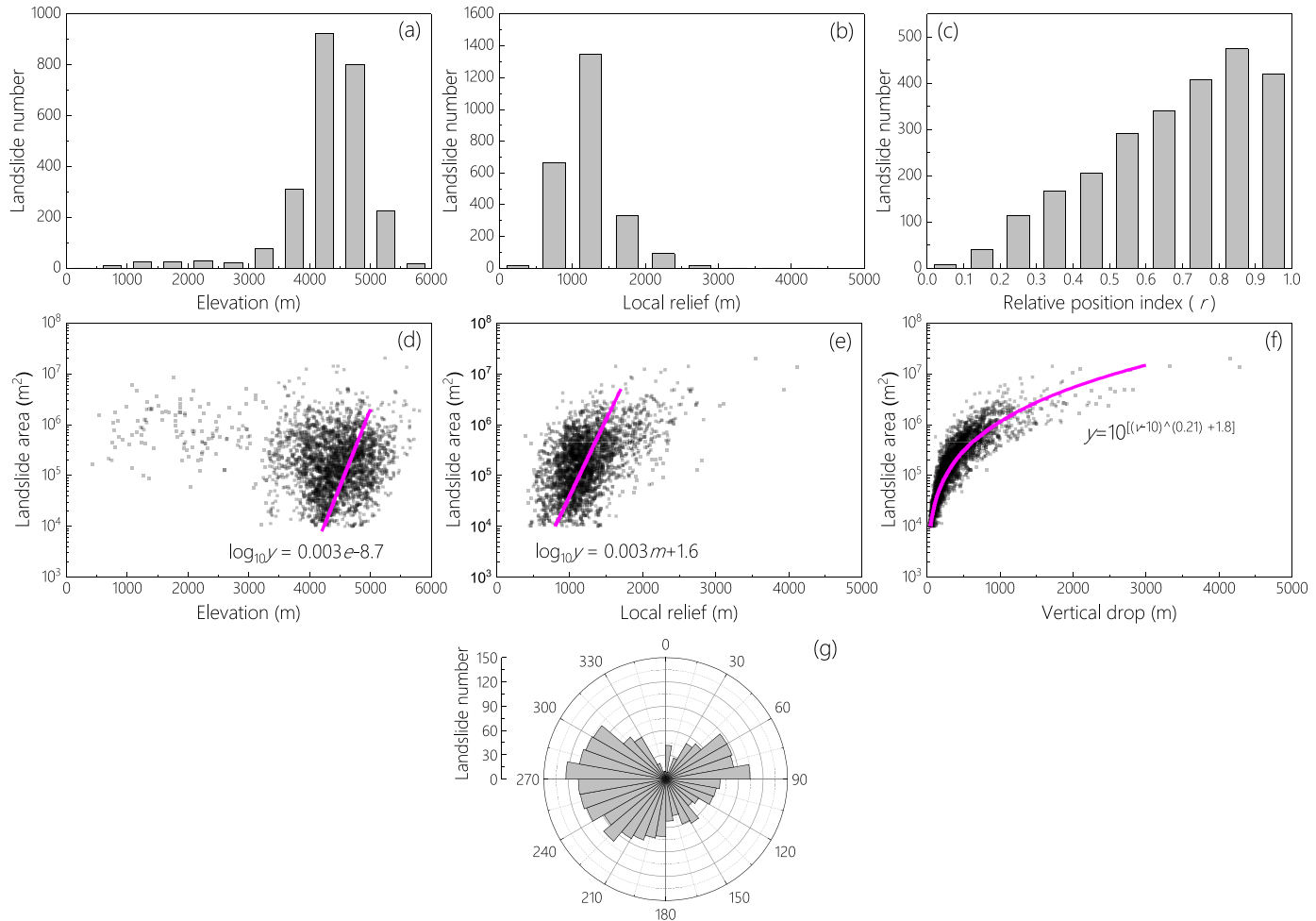


Fig. 11. (a), local relief conditions (b) and relative position index r (c); relationships between the landslide area and elevation (d); relationships between the landslide area and the local relief conditions (e); relationships between the landslide area and the elevation range (vertical drop, f); and distribution of landslide numbers for different aspects (g).

cycles, which results in intense weathering, making rocks in these areas more fractured (lower-stability state); moreover, numerous studies have suggested that permafrost could promote rock slope stability (Wei et al., 2006; Gruber and Haeberli, 2007; Wang et al., 2007; Zhou et al., 2016; Li et al., 2018). Additionally, most complex landslides in the eastern section are mainly distributed in permafrost areas (Fig. 13a), and these landslides can be characterized by a combination of MRFs and seasonal snow avalanches (Fig. 2h).

The most intense rainfall is concentrated in the lower reaches, and few landslides are distributed in this area (Fig. 13b). Here, we could not find an obvious relationship between rainfall and landslide distribution.

5. Discussion

5.1. The possible reasons for Langjiexue accretionary wedge landslide concentrations

As mentioned previously, the most obvious asymmetric distribution across the entire basin is the subtectonic unit of the Langjiexue accretionary wedge (VII₃₋₂), which is the area with the most concentrated landslides (Figs. 3 and 15) and contains 1201 landslides (48.6% of the total). However, its area covers only $1.67 \times 10^4 \text{ km}^2$, occupying 6.5% of the entire basin. Here, we summarize several potential explanations in response to this

phenomenon.

(1) Adverse geological strata play a key role. The rock groups in the YTR can be classified into four groups: hard rock, secondary hard rock, alternating hard and soft rock and soft rock. The alternating hard and soft rock is the most prone to landslides (62.6% of the total); in particular, for alternating slate and shale in the Upper Triassic Xiukang Group, more than 50% of the total rocks occur in this rock group. The alternating slate and shale cover most of zone VII₃₋₂ (Fig. 15), and approximately 92% of the landslides in zone VII₃₋₂ have occurred in this rock group. However, few landslides have occurred in the opposite bank area of the YTR under similar topographic and climate conditions but in different strata (Fig. 15). Therefore, we consider that strata (alternating slate and shale) may play a key role in determining landslide concentrations.

(2) The Tsangpo suture zone contains densely cut rocks. Zone VII₃₋₂ is part of Tsangpo suture zone VII₃, and more densely distributed faults are concentrated in zone VII₃₋₂ than in nearby subtectonic units, especially for comparison with the opposite bank area of the YTR (zones VII₁₋₆; Fig. 15). These faults (most of which are thrust faults) cut rocks densely, resulting in fractured rocks with low stability.

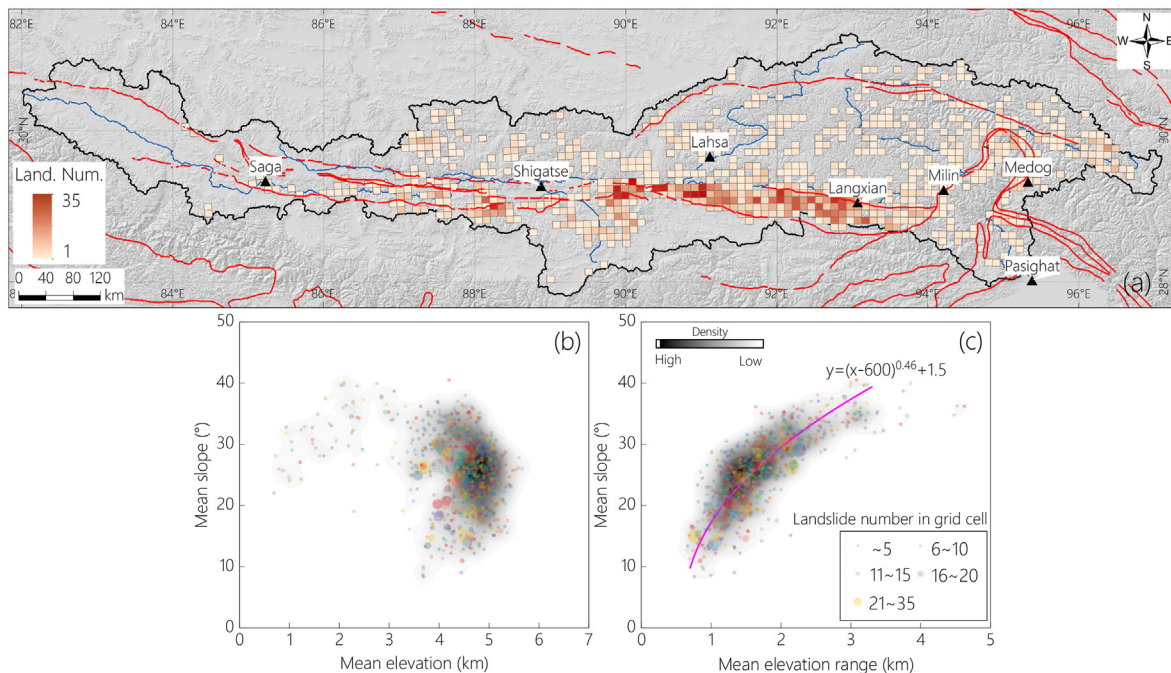


Fig. 12. Relationships between landslide concentrations and regional topographic features: (a) landslide concentration in a 10 km × 10 km cell, exhibiting the relationship between the mean slope (b) and elevation range (c). The 10 km × 10 km cells were generated using ArcGIS software, and the mean slope, mean elevation and mean elevation range were calculated in every unit cell within the 30-m resolution DEM. The circle sizes and colors correspond to landslide areas. The density reflects the concentration of grids containing landslides; a high density means that more landslides are concentrated there.

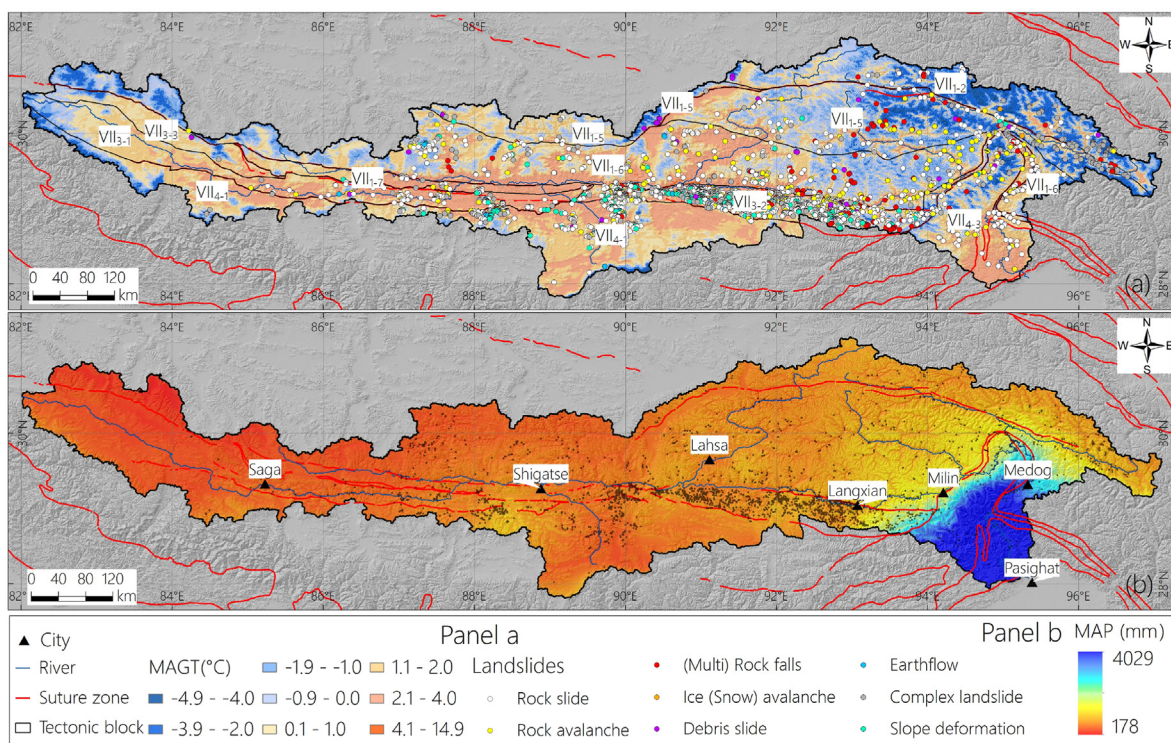


Fig. 13. Landslide distributions shown on a mean annual ground temperature (MAGT) map (a) and mean annual precipitation (MAP) map (b). The MAGT data were collected from Ran et al. (2021), the glacier data were derived from Liu et al. (2020), and the MAP data were obtained from Brocca et al. (2019).

(3) Long-term erosion continuously weakens rocks. Although alternating slate and shale strata are widely distributed along the YTR mainstream, fewer landslides have occurred in the

upstream section (VII₃₋₁), and numerous landslides are concentrated in the downstream section (VII₃₋₂) (Fig. 8c). This could be attributed to the relatively downstream section

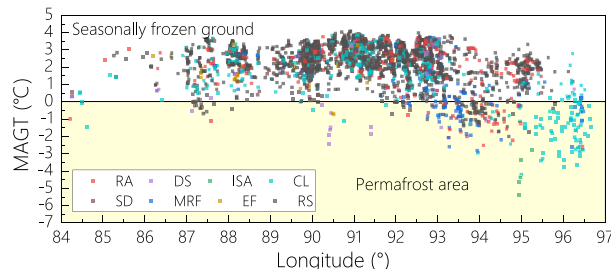


Fig. 14. Landslide distributions in different MAGT ranges.

experiencing more intense river erosion, in which intense slope foot erosion causes mountains to feature steeper topography and lower slope stability. Under the same conditions, landslides more easily reach the relative downstream section.

Additionally, in a similar scenario, adverse rock groups coupled with special tectonics make local areas prone to landslides; this scenario has also occurred in the Diexi area of the Minjin River on the eastern Tibetan Plateau (Zhao, 2020; Zhao et al., 2021b). Based on our experience in the Diexi area, we suggest additional field investigations and systematic analyses of this area to determine the reason for the difference in concentration.

5.2. Potential triggers

5.2.1. Frequent seismic activity is an important potential trigger

This landslide inventory mainly contains historical landslides for which we do not know their triggers, except for some recent cases, such as the 2000 Yigong landslide, Sedongpu glacier–rock avalanches and seismic landslides triggered by the 2017 Nyingchi earthquake. Although there remains a lack of convincing evidence proving that earthquakes are important triggers, we still consider earthquakes to be important triggers. The following are our reasons:

(1) The YTR basin and nearby areas are prone to earthquakes.

The Himalayan orogenic belt is widely accepted to be part of a typical tectonically active area, especially in the eastern Himalayan

syntaxis, and many earthquakes have occurred in this area (Fig. 16a; Holt et al., 1991; Yin and Harrison, 2000; Zhao et al., 2019c, 2021c; Coudurier-Curveur et al., 2020). At least 3000 events with magnitudes ≥ 3.0 have occurred in or near the basin since the 1900s, and the magnitudes of 84 of these events were ≥ 6.0 . The largest event was the Chayu M_w -8.6 earthquake, which occurred in 1950 (Coudurier-Curveur et al., 2020). Based on the above information, the YTR basin is part of a typical earthquake-prone area, and some past studies have confirmed this hypothesis (Coudurier-Curveur et al., 2020; Zhao et al., 2021c).

(2) Recent earthquakes have triggered numerous landslides.

Many studies have shown that seismic events play an important role in triggering landslides in tectonically active mountains (Brideau et al., 2009; Larsen and Montgomery, 2012; Du et al., 2017; Carlini et al., 2018; Görüm, 2019). These frequent seismic shaking events can cause slope stability to continuously deteriorate, resulting in easier slope collapse (Khazai and Sitar, 2004; Dai et al., 2011; Görüm et al., 2011; Fan et al., 2012; Kargel et al., 2016; Shafique et al., 2016; Massey et al., 2018; Zhao et al., 2022). For recent seismic landslides in the YTR basin, the 1950 Chayu M_w -8.6 earthquake triggered thousands of landslides and glacial avalanches (Coudurier-Curveur et al., 2020). Another example of a landslide-triggering event is the recent 2017 Nyingchi M_w -6.4 earthquake (Fig. 16b).

On 18 November 2017, a M_w -6.4 seismic event struck the eastern Himalayan syntaxis, with an epicenter located at 29.87°N, 95.02°E and a focal depth of approximately 10 km (Zhao et al., 2021c). This event triggered at least 1800 landslides and caused 3 lakes to be dammed in the meizoseismal area, and the larger cases were mainly concentrated in the upper mountains (Fig. 16b); 15 of these landslides were large landslides (these landslides were included in this inventory). Undoubtedly, numerous mega-earthquakes, such as the 1950 Chayu M_w -8.6 earthquake, have occurred within and near the basin throughout its long geological history, and this strong seismic shaking could have triggered numerous landslides, especially in some landslide-prone areas, such as the Langjixue accretionary wedge area (VII₃₋₂) and the eastern Himalayan syntaxis (Coudurier-Curveur et al., 2020). Additionally, many ancient landslides, such as the Longan Landslide, Lulang Landslide, and Nixu Landslide, have been confirmed to have been triggered by paleoearthquakes (Han, 2018; Zeng et al., 2020; Du et al., 2021).

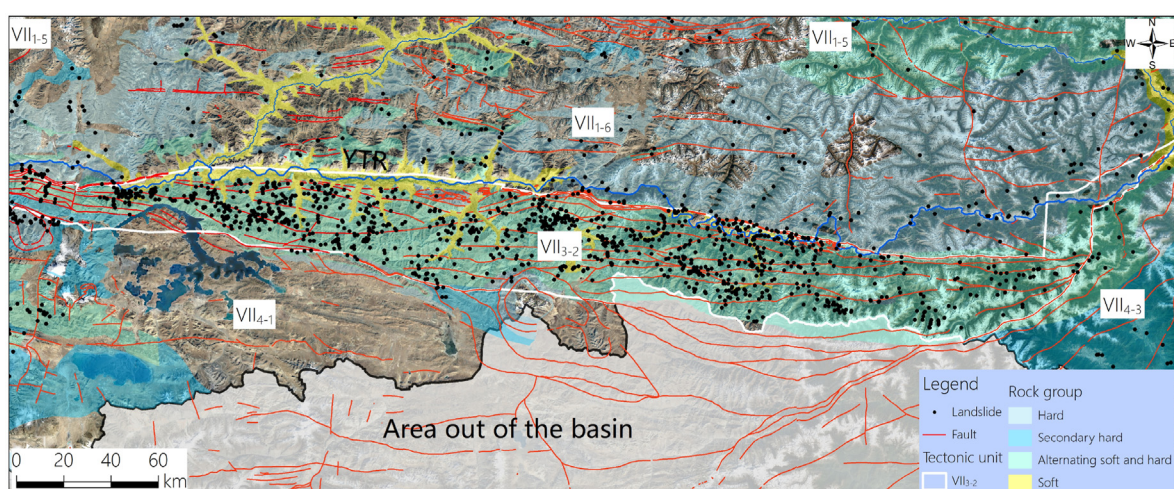


Fig. 15. Characteristics of the landslide distribution in the Langjixue accretionary wedge (VII₃₋₂). The fault is mapped from a 1:250,000 geological map.

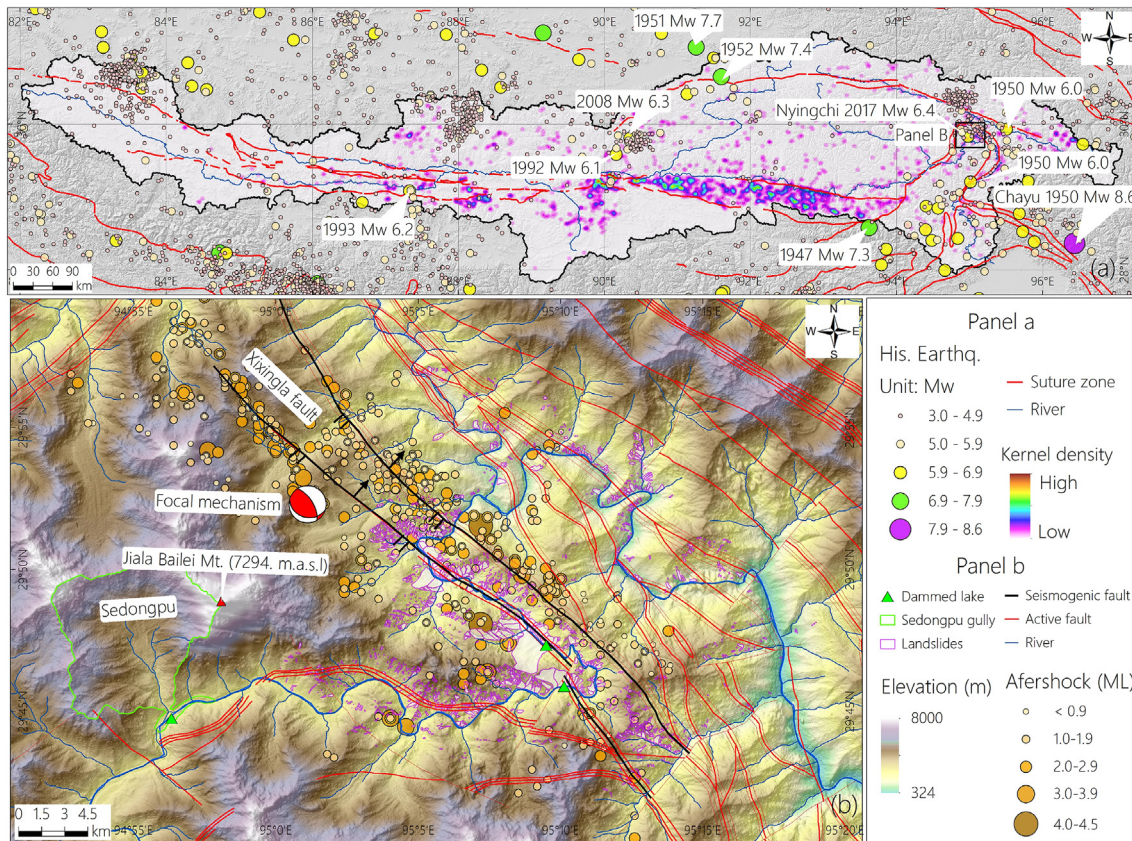


Fig. 16. Spatial distribution of historical earthquakes since 1900 (a) and distributions of aftershocks and landslides triggered by the 2017 Nyingchi M_w -6.5 earthquake (b). The historical earthquake data were obtained from the United States Geological Survey (USGS, 2023b), the Nyingchi earthquake aftershock data were collected from Yin et al. (2018), and fault and geological information (Fig. 16b) was retrieved from the 25 W geological map (CIGMR, 2003).

5.2.2. Global warming may result in more frequent ISAs

At present, many studies have verified that global warming is resulting in the retreat and degradation of glaciers and permafrost regions, especially on the Qinghai-Tibetan Plateau (Qiu, 2008; Ran et al., 2018). Several studies have also noted that glacial retreat and permafrost degradation could promote more landslides in these regions, such as the recent 2016 Aru glacier avalanches, the 2018 Sedongpu glacier–rock avalanches, and the 2021 Chamoli avalanches (Gilbert et al., 2018; Kääb et al., 2018; Shugar et al., 2021; Li et al., 2022). The Sedongpu events occurred in the YTR basin and could be a typical example (Fig. 17 and Fig. A3 in Appendix A).

Sedongpu gully is located in the eastern Himalayan syntaxis, with elevations ranging from 7174 m to 2699 m. Since October 2017, especially after the Nyingchi M_w -6.4 earthquake occurred on 17 November 2017 (the epicenter of which was located only 8 km from

the basin boundary; Fig. 16b; Zhao et al., 2021c; Li et al., 2022), Sedongpu gully has been in an active period, and at least 10 massive landslides (in which massive glaciers and rocks detached from their source areas at elevations >5000 m and rushed into gullies, reactivating massive moraines) have completely blocked the YTR according to interpretations of multiple Sentinel 2 images (Fig. 17 and Fig. A3 in Appendix A). Our previous study analyzed the relationships among the Sedongpu avalanche frequency, glacial area and average annual temperature over recent decades. The findings indicated that the temperature is consistently rising (Li et al., 2022). Continuous warming is related to the frequent collapses of fractured ice and rock masses that reactivate sediment transport belts through moraines and down into river valleys (Fig. 17).

Thus, continuous glacial retreat and permafrost degradation caused by global warming have resulted in landslides in the past

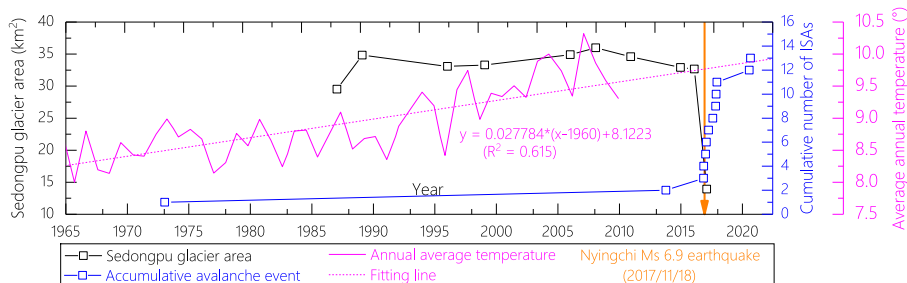


Fig. 17. Relationships among the Sedongpu glacier area, average annual temperature and cumulative ISAs (adapted from Li et al., 2022).

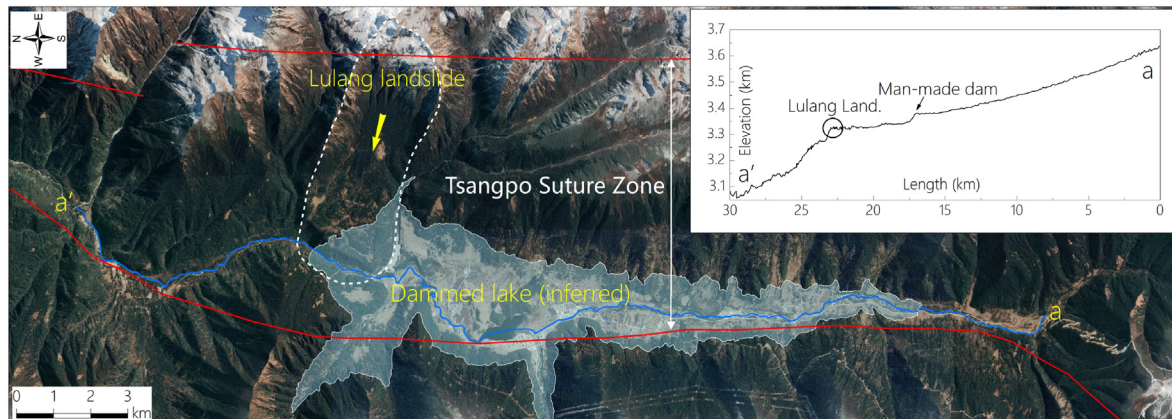


Fig. 18. Geomorphologic responses of landslide dams, showing the case study of the Lulang landslide. The location of the Lulang landslide is shown in Fig. 7.

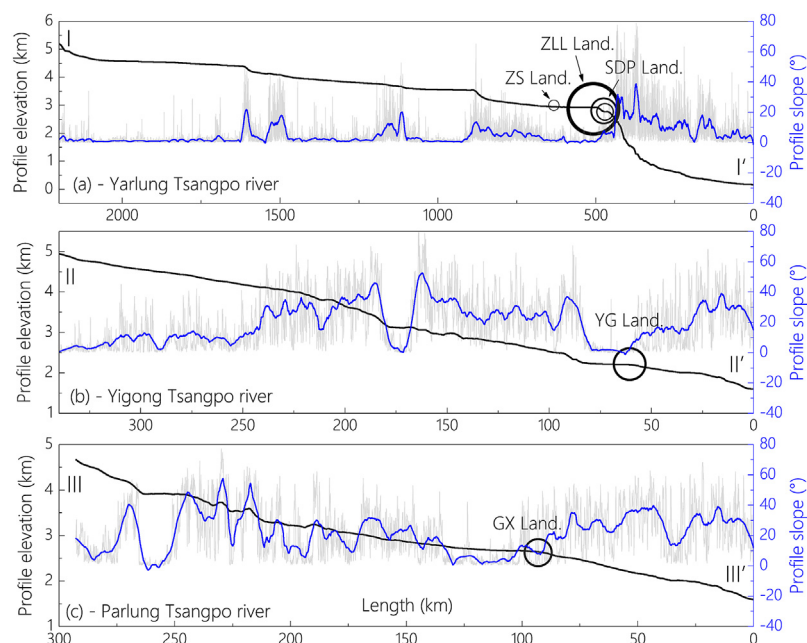


Fig. 19. River profile elevation and slope distributions and the distribution of typical landslide dams: (a) YTR, (b) YiTR, and (c) PTR. The landslide abbreviations and the locations of the river profiles are listed in Fig. 7.

and may lead to the occurrence of more ISAs in the future. However, we have evidence of only one typical Sedongpu case, and additional related evidence is urgently needed to prove this viewpoint.

5.3. Influence of landslides on the regional geomorphologic response

The large volumes associated with these forms of landslides, their rapid emplacement and the valley topography result in frequent dam formation. These dams usually block rivers and form dammed lakes, and outburst floods occur, continuously eroding the dams (Fig. 18; Korup, 2006; Fan et al., 2012). This process usually reshapes the river profile and nearby geomorphic features (Fig. 18 Wang et al., 2019).

To characterize the geomorphologic responses of landslide dams, this study constructed profiles of the mainstream YTR and two important tributaries (i.e. YiTR and PTR), as shown in Fig. 19. The figure shows that these three profiles all have several obvious knickpoints. 1) The YTR has 3 obvious controlling knickpoints, the

most obvious of which are located in the eastern Himalayan syntaxis, and repeated glacial activities (such as glacial avalanches and debris flows) in the Zelunglung gully and nearby gullies could play a vital role in these knickpoints (Fig. 19a and Fig. A4a in Appendix A; Liu et al., 2015). The nearby Sedongpu Valley has experienced high-frequency glacier–rock avalanches in recent years; these avalanches have blocked the YTR many times, and the dammed lake has remained partially stagnant. In addition, two similar landslides occurred in this region, but the scales of these landslides were much smaller than those of the Sedongpu gully landslides (Fig. 19a). A new knickpoint gradually formed at this point.

One obvious knickpoint exists in the YiTR (Fig. 19b), and this knickpoint spatially coincides with the Yigong ice–rock avalanche that occurred in the Zhamu gully (Fig. A4b in Appendix A). This landslide was also a repeated landslide (Guo et al., 2020), and historical records show that Zhamu Gully experienced at least two massive failures in 1902 and 2000, both of which completely blocked the river (Hu et al., 2021). Frequent debris flows have also temporarily blocked this point (Zou et al., 2020). All these events

caused a knickpoint to gradually form at this point. The PTR also contains one obvious knickpoint that was formed by the occurrence of multiple complex landslides in Guxiang and nearby gullies (Fig. 19b and c; Fig. A4c in Appendix A); this knickpoint has a mechanism similar to those of the previously discussed knickpoints. Based on the above information, the obvious knickpoints in the large rivers in the study area were typically formed by long-term, repeated glacial activities (Korup et al., 2010).

5.4. Limitations

Regarding landslide mapping, this study mainly focuses on historical landslides without considering the timespan, which could make the analysis of regional erosion and the influence of climate change on landslide evolution very difficult.

The landslides in this inventory are mainly historical, while several influential factors, such as the MAGT (2005–2015), the MAP (2007–2018), and seismic events (1900–2020), have occurred in recent years. These factors could result in uncertainties in the overall results. However, this approach is the only way to study related scenarios, as it is impossible to obtain such long-term relevant data.

As the area with the highest rainfall lies downstream of the eastern Himalayan syntaxis, which is among the most intense areas of erosion on Earth, fewer landslide scenarios occur here; thus, we recognize few landslides in the area with the highest rainfall and do not find a relationship between rainfall and landslide distribution.

Finally, additional detailed studies, including collections of more precise geological, topographic and climate data; a systematic field investigation of the characteristics of the detailed tectonic setting, rock integrity, failure mechanism, etc., and further analysis of additional potential factors affecting the landslide distribution, need to be carried out. After finishing these, the systematical landslide susceptibility, which takes complex geo-environments into consideration, can be the next study major.

6. Conclusions

Given the lack of understanding of the spatial and size distributions of the entire YTR basin, this study established a landslide inventory for the YTR basin and evaluated the spatial and size distributions of the identified landslides. The following conclusions can be summarized.

- (1) A total of 2390 landslides were identified in the YTR basin and could be classified into eight types of rockslides (1270, 53.1%), rock avalanches (281, 11.8%), multi-rock falls (127, 5.3%), ice–snow avalanches (5, 0.2%), debris slides (46, 1.9%), earthflows (31, 1.3%), complex landslides (435, 18.2%), and slope deformations (195, 8.2%). These landslides covered a volume of 48.4 km³.
- (2) The distributions of these landslides were highly asymmetric, including the Tsangpo suture zone (occupying 53.4% of the total), which contained more landslides than other tectonic units, especially in the subzone of the Langjixue accretionary wedge (VII_{3.2}). The alternating hard and soft rock groups contained more landslides than the other rock groups.
- (3) The area south of the middle reaches contained a higher concentration of landslides than did the other regions. The relief and elevation conditions controlled the landslide size, and positive relationships were found between the local relief and landslide area and between the elevation range and landslide area, both of which exhibited positive exponential functions. The landslide distribution had no obvious

relationship with rainfall, and seasonally frozen ground caused more landslides to concentrate.

- (4) Alternating slate and shale (alternating between hard and soft rock groups) in the Tsangpo suture zone could be the factor responding to landslide concentration. A total of 20.6% of the landslides once obviously blocked rivers, 45 landslides still obviously dam lakes or sediments, and some had formed river knickpoints. Finally, although there remains a lack of convincing evidence suggesting that earthquakes are important triggers, we still consider earthquakes to be an important trigger. Due to the limited data, spatial and size analyses are perhaps immature, and further systematic analysis is needed.

Data availability

The supplementary figures (Figs. S1–S4) and supplementary table (Table S1) used in this work are available in Appendix A. The detailed landslide information is available in Appendix B “Detailed landslide information” Excel file. Other data are available upon request from the first author.

Declaration of competing interest

The authors declare that they have no known competing financial interests or personal relationships that could have appeared to influence the work reported in this paper.

Acknowledgments

This research is supported by the National Key R&D Program of China (Grant No. 2023YFC3008300), the Science and Technology Research Program of the Institute of Mountain Hazards and Environment, Chinese Academy of Sciences, Chinese Academy of Sciences (Grant No. IMHE-ZYTS-03 and IMHE-ZDRW-03). The authors express their gratitude for this financial assistance. We also thank the editor and two anonymous reviewers for their constructive comments, which significantly improved the quality of this work.

Appendix A. Supplementary data

Supplementary data to this article can be found online at <https://doi.org/10.1016/j.jrmge.2024.01.021>.

References

- Agliardi, F., Crosta, G., Zanchi, A., 2001. Structural constraints on deep-seated slope deformation kinematics. *Eng. Geol.* 59 (1–2), 83–102.
- AW3D30, 2024. ALOS global digital surface model "ALOS world 3D - 30m (AW3D30)". https://www.eorc.jaxa.jp/ALOS/en/dataset/aw3d30/aw3d30_e.htm. (Accessed 10 February 2023).
- Bloom, C.K., MacInnes, B., Higman, B., et al., 2020. Catastrophic landscape modification from a massive landslide tsunami in Taan Fiord, Alaska. *Geomorphology* 353, 107029.
- Brideau, M.A., Yan, M., Stead, D., 2009. The role of tectonic damage and brittle rock fracture in the development of large rock slope failures. *Geomorphology* 103 (1), 30–49.
- Brocca, L., Filippucci, P., Hahn, S., et al., 2019. SM2RAIN–ASCAT (2007–2018): global daily satellite rainfall data from ASCAT soil moisture observations. *Earth Syst. Sci. Data* 11 (4), 1583–1601.
- Carlini, M., Chelli, A., Vescovi, P., et al., 2016. Tectonic control on the development and distribution of large landslides in the Northern Apennines (Italy). *Geomorphology* 253, 425–437.
- Carlini, M., Chelli, A., Francese, R., et al., 2018. Landslides types controlled by tectonics-induced evolution of valley slopes (Northern Apennines, Italy). *Landslides* 15 (2), 283–296.
- CIGMR, 2003. Geological Map of Medog County (1:25w). Map No. H46C003004. Chengdu Institute of Geology and Mineral Resources (In Chinese).
- Coudurier-Curver, A., Tapponnier, P., Okal, E., et al., 2020. A composite rupture

- model for the great 1950 Assam earthquake across the cusp of the East Himalayan Syntaxis. *Earth Planet Sci. Lett.* 531, 115928.
- Cruden, D.M., Varnes, D.J., 1996. Landslide types and processes. Special Report 247. In: Turner, A.K., Schuster, R.L. (Eds.), *Landslides Investigation and Mitigation*. Transportation research board, US National Research Council, Washington, DC, pp. 36–75 (Chapter 3).
- Dai, F.C., Xu, C., Yao, X., et al., 2011. Spatial distribution of landslides triggered by the 2008 M 8.0 Wenchuan earthquake, China. *J. Asian Earth Sci.* 40 (4), 883–895.
- Delaney, K.B., Evans, S.G., 2015. The 2000 Yigong landslide (Tibetan Plateau), rockslide-dammed lake and outburst flood: review, remote sensing analysis, and process modelling. *Geomorphology* 246, 377–393.
- Deng, Q.D., Cheng, S.P., Ji, M., Peng, D., 2014. Seismic activities and earthquake potential in the Tibetan Plateau. *Chin. J. Geophys.* 57 (5), 678–697 (In Chinese with English abstract).
- Du, G., Zhang, Y., Yang, Z., et al., 2017. Estimation of seismic landslide Hazard in the eastern Himalayan Syntaxis region of Tibetan plateau. *Acta Geol. Sin. Engl.* 91 (2), 658–668.
- Du, G., Zhang, Y., Yang, Z., et al., 2019. Landslide susceptibility mapping in the region of eastern Himalayan syntaxis, Tibetan Plateau, China: a comparison between analytical hierarchy process information value and logistic regression-information value methods. *Bull. Eng. Geol. Environ.* 78 (6), 4201–4215.
- Du, G.L., Zhang, Y.S., Yao, X., Yang, Z.H., Yuan, Y., 2021. Field investigations and numerical modeling of a giant landslide in the region of Eastern Himalayan Syntaxis: jiaobunong landslide. *J. Mt. Sci.* 18 (12), 3230–3246.
- Elliott, J.R., Jolivet, R., González, P.J., et al., 2016. Himalayan megathrust geometry and relation to topography revealed by the Gorkha earthquake. *Nat. Geosci.* 9 (2), 174–180.
- Fan, X., van Westen, C.J., Xu, Q., Gorum, T., Dai, F., 2012. Analysis of landslide dams induced by the 2008 Wenchuan earthquake. *J. Asian Earth Sci.* 57, 25–37.
- Finnegan, N.J., Hallet, B., Montgomery, D.R., et al., 2008. Coupling of rock uplift and river incision in the namche barwa–guala peri massif, tibet. *Geol. Soc. Am. Bull.* 120 (1–2), 142–155.
- Gilbert, A., Leinss, S., Kargel, J., et al., 2018. Mechanisms leading to the 2016 giant twin glacier collapses, Aru Range, Tibet. *Cryosphere* 12 (9), 2883–2900.
- GB 50021-2001, 2009. *Code for Investigation of Geotechnical Engineering*, GB. Ministry of construction, China.
- Görüm, T., Fan, X., van Westen, C.J., et al., 2011. Distribution pattern of earthquake-induced landslides triggered by the 12 May 2008 Wenchuan earthquake. *Geomorphology* 133 (3–4), 152–167.
- Görüm, T., 2019. Tectonic, topographic and rock-type influences on large landslides at the northern margin of the Anatolian Plateau. *Landslides* 16 (2), 333–346.
- Gruber, S., Haeblerli, W., 2007. Permafrost in steep bedrock slopes and its temperature-related destabilization following climate change. *J. Geophys. Res-Earth* 112 (F2).
- Guo, C., Montgomery, D.R., Zhang, Y., et al., 2020. Evidence for repeated failure of the giant Yigong landslide on the edge of the Tibetan Plateau. *Sci. Rep.* 10 (1), 1–7.
- Han, L.M., 2018. Geological Hazard Characteristics and Risk Assessment of Brahmaputra from Wolong to Zhibai Stream Segment. Chengdu University of Technology, Master Thesis (In Chinese with English abstract).
- Heidbach, O.M., Rajabi, X., Cui, K., et al., 2018. The World Stress Map database release 2016: crustal stress pattern across scales. *Tectonophysics* 744, 484–498.
- Hewitt, K., 2009. Catastrophic rock slope failures and late quaternary developments in the Nanga parbat–haramosh massif, upper Indus Basin, northern Pakistan. *Quat. Sci. Rev.* 28 (11–12), 1055–1069.
- Highland, L., Bobrowsky, P.T., 2008. *The Landslide Handbook: a Guide to Understanding Landslides*. US Geological Survey, Reston, p. 129.
- Holt, W.E., Ni, J.F., Wallace, T.C., Haines, A.J., 1991. The active tectonics of the eastern Himalayan syntaxis and surrounding regions. *J. Geophys. Res. Solid Earth* 96 (B9), 14595–14632.
- Hovius, N., Stark, C.P., Allen, P.A., 1997. Sediment flux from a mountain belt derived by landslide mapping. *Geology* 25 (3), 231–234.
- Hu, K., Wu, C., Wei, L., et al., 2021. Geomorphic effects of recurrent outburst superfloods in the Yigong River on the southeastern margin of Tibet. *Sci. Rep.* 11 (1), 1–11.
- Hung, O., Leroueil, S., Picarelli, L., 2014. The Varnes classification of landslide types, an update. *Landslides* 11 (2), 167–194.
- Jia, H., Wang, Y., Ge, D., Deng, Y., Wang, R., 2020. Improved offset tracking for predisaster deformation monitoring of the 2018 Jinsha River landslide (Tibet, China). *Remote Sens. Environ.* 247, 111899.
- Kääb, A., Leinss, S., Gilbert, A., et al., 2018. Massive collapse of two glaciers in western Tibet in 2016 after surge-like instability. *Nat. Geosci.* 11 (2), 114–120.
- Kargel, J.S., Leonard, G.J., Shugar, D.H., et al., 2016. Geomorphic and geologic controls of geohazards induced by Nepal's 2015 Gorkha earthquake. *Science* 351 (6269), aac8353.
- Keeler, D.K., 2002. Investigating landslides caused by earthquakes—a historical review. *Surv. Geophys.* 23 (6), 473–510.
- Khazai, B., Sitar, N., 2004. Evaluation of factors controlling earthquake-induced landslides caused by Chi-Chi earthquake and comparison with the Northridge and Loma Prieta events. *Eng. Geol.* 71 (1–2), 79–95.
- Korup, O., 2005. Distribution of landslides in southwest New Zealand. *Landslides* 2 (1), 43–51.
- Korup, O., 2006. Rock-slope failure and the river long profile. *Geology* 34 (1), 45–48.
- Korup, O., Clague, J.J., Hermanns, R.L., et al., 2007. Giant landslides, topography, and erosion. *Earth Planet Sci. Lett.* 261 (3–4), 578–589.
- Korup, O., Montgomery, D.R., 2008. Tibetan plateau river incision inhibited by glacial stabilization of the Tsangpo gorge. *Nature* 455 (7214), 786–789.
- Korup, O., Montgomery, D.R., Hewitt, K., 2010. Glacier and landslide feedbacks to topographic relief in the Himalayan syntaxes. *Proc. Natl. Acad. Sci. USA* 107 (12), 5317–5322.
- Lang, K.A., Huntington, K.W., Montgomery, D.R., 2013. Erosion of the Tsangpo gorge by megafloods, eastern himalaya. *Geology* 41 (9), 1003–1006.
- Larsen, I.J., Montgomery, D.R., Korup, O., 2010. Landslide erosion controlled by hillslope material. *Nat. Geosci.* 3 (4), 247–251.
- Larsen, I.J., Montgomery, D.R., 2012. Landslide erosion coupled to tectonics and river incision. *Nat. Geosci.* 5 (7), 468–473.
- Li, J., Zhou, K., Liu, W., Zhang, Y., 2018. Analysis of the effect of freeze–thaw cycles on the degradation of mechanical parameters and slope stability. *Bull. Eng. Geol. Environ.* 77 (2), 573–580.
- Li, W., Zhao, B., Xu, Q., et al., 2022. More frequent glacier-rock avalanches in Sedongpu gully are blocking the Yarlung Zangbo River in eastern Tibet. *Landslides* 1–13.
- Li, W., Lai, Z., Hu, K., et al., 2015. Age and extent of a giant glacial-dammed lake at Yarlung Tsangpo gorge in the Tibetan Plateau. *Geomorphology* 246, 370–376.
- Liu, X., Xu, Z., Yang, H., Li, X., Peng, D., 2020. Consolidating the Randolph glacier inventory and the glacier inventory of China over the Qinghai-Tibetan Plateau and investigating glacier changes since the mid-20th century. *Earth Syst. Sci. Data Discuss.* <https://doi.org/10.5194/esd-2020-71>, 2020.
- Malamud, B.D., Turcotte, D.L., Guzzetti, F., Reichenbach, P., 2004. Landslides, earthquakes, and erosion. *Earth Planet Sci. Lett.* 229 (1–2), 45–59.
- Marc, O., Behling, R., Andermann, C., et al., 2019. Long-term erosion of the Nepal Himalayas by bedrock landsliding: the role of monsoons, earthquakes and giant landslides. *Earth Surf. Dyn.* 7 (1), 107–128.
- Massey, C., Townsend, D., Rathje, E., et al., 2018. Landslides triggered by the 14 November 2016 M w 7.8 Kaikōura earthquake, New Zealand. *Bull. Seismol. Soc. Am.* 108 (3B), 1630–1648.
- Ouimet, W.B., 2010. Landslides associated with the May 12, 2008 Wenchuan earthquake: implications for the erosion and tectonic evolution of the Longmen Shan. *Tectonophysics* 491 (1–4), 244–252.
- Pan, G.T., Li, X.Z., Wang, L.Q., Ding, J., Chen, Z.L., 2002. Preliminary division of tectonic units of the Qinghai-Tibet Plateau and its adjacent regions. *Regional Geology of China* (11), 701–707.
- Pánek, T., Břežný, M., Kilnar, J., Winocur, D., 2021. Complex causes of landslides after ice sheet retreat: post-LGM mass movements in the Northern Patagonian Ice-field region. *Sci. Total Environ.* 758, 143684.
- Qiu, J., 2008. The third pole: climate change is coming fast and furious to the Tibetan plateau. Jane Qiu reports on the changes atop the roof of the world. *Nature* 454 (7203), 393–397.
- Ran, Y., Li, X., Cheng, G., 2018. Climate warming over the past half century has led to thermal degradation of permafrost on the Qinghai–Tibet Plateau. *Cryosphere* 12 (2), 595–608.
- Ran, Y., Li, X., Cheng, G., et al., 2021. Mapping the permafrost stability on the Tibetan Plateau for 2005–2015. *Sci. China Earth Sci.* 64 (1), 62–79.
- Roback, K., Clark, M.K., West, A.J., et al., 2018. The size, distribution, and mobility of landslides caused by the 2015 M_w7.8 Gorkha earthquake, Nepal. *Geomorphology* 301, 121–138.
- Roering, J., 2012. Landslides limit mountain relief. *Nat. Geosci.* 5 (7), 446–447.
- Shafique, M., van der Meijde, M., Khan, M.A., 2016. A review of the 2005 Kashmir earthquake-induced landslides; from a remote sensing prospective. *J. Asian Earth Sci.* 118, 68–80.
- Shugar, D.H., Jacquemart, M., Shean, D., et al., 2021. A massive rock and ice avalanche caused the 2021 disaster at Chamoli, Indian Himalaya. *Science* 373 (6552), 300–306.
- Tanyaş, H., van Westen, C.J., Allstadt, K.E., Jibson, R.W., 2019. Factors controlling landslide frequency-area distributions. *Earth Surf. Process. Landforms* 44 (4), 900–917.
- Tebbens, S.F., 2020. Landslide scaling: a review. *Earth Space Sci.* 7 (1), e2019EA000662.
- USGS, 2023a. Plate boundaries. <https://www.usgs.gov/media/files/plate-boundaries-kmz-file>. (Accessed 10 February 2023).
- USGS, 2023b. Global earthquake inventory. <https://earthquake.usgs.gov/earthquakes/map/>. (Accessed 5 February 2023).
- Wang, D.Y., Ma, W., Niu, Y.H., Chang, X.X., Wen, Z., 2007. Effects of cyclic freezing and thawing on mechanical properties of Qinghai–Tibet clay. *Cold Reg. Sci. Technol.* 48 (1), 34–43.
- Wang, Y., Zhao, B., Li, J., 2018. Mechanism of the catastrophic June 2017 landslide at Xinmo village, Songping river, Sichuan province, China. *Landslides* 15 (2), 333–345.
- Wang, H., Cui, P., Liu, D., et al., 2019. Evolution of a landslide-dammed lake on the southeastern Tibetan Plateau and its influence on river longitudinal profiles. *Geomorphology* 343, 15–32.
- Wang, Y., Cheng, Q., Lin, Q., et al., 2023. Rock avalanches in the Tibetan plateau of China. In: *Progress in Landslide Research and Technology*, 2. Springer Nature Switzerland, Cham, pp. 55–111. Issue 2, 2023.
- Wei, M., Fujun, N., Satoshi, A., Dewu, J., 2006. Slope instability phenomena in permafrost regions of Qinghai-Tibet Plateau, China. *Landslides* 3 (3), 260–264.
- Wen, B., Wang, S., Wang, E., Zhang, J., 2004. Characteristics of rapid giant landslides in China. *Landslides* 1 (4), 247–261.
- Wu, J.F., 2013. *Research on Development Characteristics and Genetic Mechanism of the Seismic Landslide in Dadu River*. PhD Thesis. Chengdu University of

- Technology, Chengdu, China (in Chinese).
- Xu, Q., Zhao, B., Dai, K., et al., 2023. Remote sensing for landslide investigations: a progress report from China. Eng. Geol. 107156.
- Yin, A., Harrison, T.M., 2000. Geologic evolution of the Himalayan-Tibetan orogen. Annu. Rev. Earth Planet Sci. 28 (1), 211–280.
- Yin, X.Z., Zhou, B.G., Chen, J.H., et al., 2018. Spatial-temporal distribution characteristics of early aftershocks following the M6.9 Mainling earthquake in Tibet, China. Chin. J. Geophys. 61 (6), 2322–2331.
- Zeng, Q., Yuan, G., McSaveney, M., et al., 2020. Timing and seismic origin of Nixu rock avalanche in southern Tibet and its implications on Nimu active fault. Engin. Geol. 268, 105522.
- Zeng, Q., Zhu, J., Liao, L., et al., 2021. High mobility of the channelized ancient Linka rock avalanche within the Bangong-Nujiang suture zone, SE Tibetan Plateau. Eng. Geol. 282, 105999.
- Zhao, J., Yuan, X., Liu, H., et al., 2010. The boundary between the Indian and Asian tectonic plates below Tibet. Proc. Natl. Acad. Sci. USA 107 (25), 11229–11233.
- Zhao, B., Wang, Y., Chen, M., et al., 2019a. Typical characteristics of large-scale landslides in the transition belt between the Qinghai-Tibet Plateau and the Loess Plateau. Arabian J. Geosci. 12, 1–10.
- Zhao, B., Li, W., Wang, Y., Lu, J., Li, X., 2019b. Landslides triggered by the M_s 6.9 Nyingchi earthquake, China (18 November 2017): analysis of the spatial distribution and occurrence factors. Landslides 16 (4), 765–776.
- Zhao, B., 2020. The Mechanism of Large Earthquake-Triggered Landslides in Area of High Intensity and Deep Canyon of Northwest Sichuan. PhD Thesis. Chengdu University of Technology, Chengdu, China (in Chinese).
- Zhao, G.M., Wu, Z.H., Liu, J., Zhang, L., Zuo, J.M., 2019c. The time space distribution characteristics and migration law of large earthquakes in the Indian-Eurasian plate collision deformation area. J. Geom. 25 (3), 324–340.
- Zhao, B., Wang, Y., Wu, J., et al., 2021a. The Mogangding giant landslide triggered by the 1786 Moxi M 7.75 earthquake, China. Nat. Hazards 106 (1), 459–485.
- Zhao, B., Wang, Y.S., Li, J., Wang, J.L., Tang, C.X., 2021b. Insights into a giant landslide-prone area on the eastern margin of the Tibetan Plateau, China. J. Mt. Sci. 18 (1), 21–37.
- Zhao, B., Wang, Y., Li, W., et al., 2021c. Insights into the geohazards triggered by the 2017 M_s 6.9 Nyingchi earthquake in the east Himalayan syntaxis, China. Catena 205, 105467.
- Zhao, B., Hu, K.H., Yang, Z.J., et al., 2022. Geomorphic and tectonic controls of landslides induced by the 2022 Luding earthquake. J. Mt. Sci. 19 (12), 3323–3345.
- Zhao, B., Su, L., Wang, Y., Li, W., Wang, L., 2023a. Insights into some large-scale landslides in southeastern margin of Qinghai-Tibet Plateau. J. Rock Mech. Geotech. 15 (8), 1960–1985.
- Zhao, B., Su, L., Xu, Q., et al., 2023b. A review of recent earthquake-induced landslides on the Tibetan Plateau. Earth Sci. Rev. 104534.
- Zhao, B., 2024. Climatological and geological controls on seismic earthflows in coastal areas. Catena 235, 107692.
- Zhou, J.W., Cui, P., Yang, X.G., 2013. Dynamic process analysis for the initiation and movement of the Donghekou landslide-debris flow triggered by the Wenchuan earthquake. J. Asian Earth Sci. 76, 70–84.
- Zhou, J.W., Cui, P., Hao, M.H., 2016. Comprehensive analyses of the initiation and entrainment processes of the 2000 Yigong catastrophic landslide in Tibet, China. Landslides 13 (1), 39–54.
- Zhou, L., Liu, W., Chen, X., et al., 2021. Relationship between dams, knickpoints and the longitudinal profile of the Upper Indus River. Front. Earth Sci. 9, 660996.
- Zou, D., Zhao, L., Sheng, Y., et al., 2017. A new map of permafrost distribution on the Tibetan Plateau. Cryosphere 11 (6), 2527–2542.
- Zou, Q., Cui, P., Jiang, H., et al., 2020. Analysis of regional river blocking by debris flows in response to climate change. Sci. Total Environ. 741, 140262.



Bo Zhao received his PhD in Geological Engineering from The Chengdu University of Technology, China, in 2019. He is currently an associate research fellow at the Institute of Mountain Hazards and Environment, Chinese Academy of Sciences. His research interests include (1) regional landslide evolution; (2) mechanism of large landslides; and (3) GIS and landslides. He has already published over 30 papers in international journals.



Lijun Su received his PhD degree in civil engineering from the Hong Kong Polytechnic University in 2006. From 2008 to 2011, he was a research fellow at the University of Wollongong. Since 2012, he has worked at the Institute of Mountain Hazards and Environment, Chinese Academy of Sciences. He is currently a professor and affiliated as Deputy Director General of the Institute of Mountain Hazards and Environment, Chinese Academy of Sciences. His expertise is in Geotechnical Mechanics and the mechanism and mitigation of landslides. He is a board member of the *International Consortium on Landslides* and executive board member of the division for landslides and engineering slopes of the Chinese Society for Rock Mechanics and Engineering. He also works for several international journals as an editor, such as *Journal of Mountain Science*. He has already published over 100 papers in international journals.